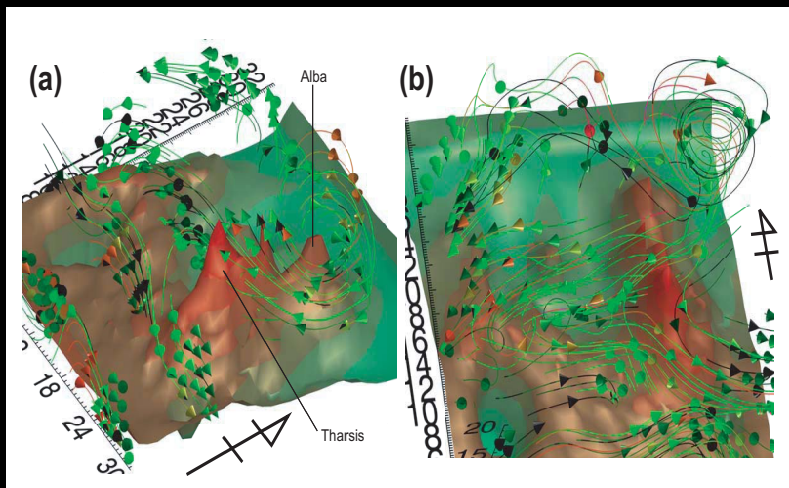


Influence of the Surface on the Atmospheric Circulation of Mars: Study with a General Circulation Model



Ryu Saito

International Max Planck Research School
on Physical Processes in the Solar System and Beyond
at the Universities of Braunschweig and Göttingen

Influence of the Surface on the Atmospheric Circulation of Mars: Study with a General Circulation Model

Von der Fakultät für Physik
der Technischen Universität Carolo-Wilhelmina
zu Braunschweig
zur Erlangung des Grades eines
Doktors der Naturwissenschaften
(Dr.rer.nat.)
genehmigte
Dissertation

von Ryu Saito
aus Toyama / Japan

Bibliografische Information Der Deutschen Bibliothek

Die Deutsche Bibliothek verzeichnet diese Publikation in der Deutschen Nationalbibliografie; detaillierte bibliografische Daten sind im Internet über <http://dnb.ddb.de> abrufbar.

1. Referentin oder Referent: Prof. Dr. Karl-Heinz Glaßmeier

2. Referentin oder Referent: Prof. Dr. Franz-Josef Lübken

eingereicht am: 21. April 2006

mündliche Prüfung (Disputation) am: 4. Juli 2006

Copyright © Copernicus GmbH 2007

ISBN 978-3-936586-72-5

Copernicus GmbH, Katlenburg-Lindau

Druck: Schaltungsdienst Lange, Berlin

Printed in Germany

Contents

Contents	3
Abstract	5
1 Introduction	7
1.1 The Martian Orbit and Climate	7
1.2 The Martian Surface	7
1.3 The Martian Atmosphere	8
1.4 Atmospheric Waves	9
1.5 Scientific Motivation	12
2 Model Description	15
2.1 Basic Equations	17
2.2 Frictional Effects	18
2.3 The Convective Adjustment	19
2.4 The Radiation Balance	20
2.4.1 Longwave Radiation	20
2.4.2 Solar Radiation	23
2.4.3 Energy Budget at the Surface	23
2.5 Discretization and Parameterization	25
3 Simulation Results	27
3.1 Solar Tides	28
3.2 Thermally Forced Stationary Planetary Waves	30
3.3 Mechanically Forced Stationary Planetary Waves	34
3.4 Simulation with all Types of Waves Included	39
3.5 Baroclinic Waves	39
3.6 The Influence of the Topography on Wave Propagation	43
3.7 The Influence of the Topography on the Mean Circulation	44
3.8 The Local Circulation Induced by Mountains	46
3.9 The Surface Temperature	52
3.10 The Influence of the Polar Caps	54
4 Comparison of the Simulations with Measurements	61
4.1 Introduction	61
4.2 The Zonal Mean Temperature	61
4.3 Longitudinal Disturbances in Mid- and High Latitudes	63

4.4 The Relation of the Surface Temperature with the Thermal Inertia and Albedo	65
5 Conclusions	69
A List of Principal Symbols	71
Bibliography	73
Acknowledgements	81

Abstract

Unlike on Earth where 3/4 of the surface is covered by oceans, the Martian surface has rougher topography with greater magnitudes of mountains and valleys. The Martian atmosphere is less dense compared to the terrestrial one. The planetary boundary layer is significantly shallower on Mars than on Earth. These differences indicate that the Martian atmosphere should be very sensitive to the forcing from below. The major mechanism which provides vertical coupling are atmospheric waves generated in the lower atmosphere near the surface. These waves transport the momentum, energy, and heat away from places of their generation in the lower atmosphere. Propagating upward the wave disturbances grow in amplitude, and ultimately break or dissipate. They release the wave energy and momentum to the zonal mean circulation, and thus affect the global transport in the atmosphere of Mars. The main task of this work is to study various physical phenomena which take place in the atmosphere near the surface with an emphasis on the mechanisms of wave generation. Effects of the large scale longitudinal disturbances on the general circulation, especially in the upper and middle atmosphere, are explored. Results of numerical experiments with the General Circulation Model of the Martian Atmosphere (MAOAM) show the sensitivity of the zonal mean circulation to the surface properties. Planetary waves of different scales are generated by a flow over the topography as well as by the inhomogeneous reaction of the surface and the lower atmospheric layers to the solar heating. Solar tides are excited by the diurnal variations in the solar energy absorption by the air, and especially, by the surface. These large scale disturbances propagate upward and horizontally according to the selective transmission properties of the atmosphere, and redistribute the wave momentum and energy. Breaking waves provide a torque to the mean zonal wind and maintain the global meridional transport. The results of the numerical simulations showing the sensitivity of the polar night jet to the topography, the inhomogeneous thermal inertia and the surface albedo, are presented here. In order to validate the simulations, the numerical results are compared with observations from the Thermal Emission Spectrometer (TES) onboard the Mars Global Surveyor (MGS). This work was a part of the ongoing Martian Atmosphere Observations And Modeling (MAOAM) project to develop and validate a comprehensive state-of-the-art general circulation model of the Martian atmosphere.

1 Introduction

1.1 The Martian Orbit and Climate

Basic planetary parameters of Mars are summarized in Table 1.1 [Lewis *et al.*, 1999; Leovy, 2001] in comparison to Earth. According to this table, the Martian diameter is approximately two times smaller than the terrestrial one, while the Martian orbital period is about 2 terrestrial years long. The rotational periods of Mars and Earth are very close, and both rotational axes are tilted by a similar degree. This means that there are seasons on Mars, pretty much the same as on Earth.

The orbit of Mars has a significant eccentricity (Figure 1.1) compared to Earth. The distance to the Sun during the aphelion is 1.2 times larger than during the perihelion. This orbital asymmetry strongly affects the seasons and climate of Mars. Northern summers occur near the aphelion, i.e. for the solar longitude or $L_s = 90^\circ$. They last longer due to the orbit characteristics, but generally are colder, while southern summers occur near the perihelion ($L_s = 270^\circ$). Although these summers are hotter, they last shorter.

The averaged surface temperature of the planet is around 218 K, but the instantaneous surface temperature varies from as low as ≈ 140 K during a nighttime in winters to as high as ≈ 300 K during a daytime in summers. Dust storms most often occur in the atmosphere of Mars during southern summers ($L_s = 270^\circ$), and have a profound effect on the temperature and circulation, especially below the mesosphere. The global mean temperature profile on Mars in Figure 1.3 (dotted line) is shifted noticeably to high values during dusty seasons.

1.2 The Martian Surface

Mars has very rough and jugged surface [Jakosky and Phillips, 2001]. It is probably the most irregular terrain among the planets of the Earth-type group. There are many outstanding features on the Martian surface [Smith and Zuber, 1996].

One of them is Olympus Mons in Figure 1.2. It is the greatest mountain in the solar system. It rises up from the surrounding plains to 25–27 km. Its bottom is about 500 km or more in diameter. The other prominent mountains are located in the Tharsis region and feature the volcanoes Ascraeus Mons, Pavonis Mons and Arsia Mons, which are almost as high as Olympus Mons. There are huge gorge systems, like the up to 8 km deep Marineris Canyon which extends for about 4000 km. Almost all the surface is covered by craters, like the 6 km deep and 2000 km in diameter Hellas basin, rift valleys, mountain ranges, hills, and plains. The Southern hemisphere is a rugged high ground with a lot of craters [Smith *et al.*, 1999].

Table 1.1: Fact sheet of comparison between Mars and Earth. Note that the Martian axis tilt and rotation period are very similar to Earth ones. Besides, Mars has also seasonal and diurnal variation against the atmosphere. However the orbit eccentricity is quite different. The values are based on *Leovy*, [2001].

	Earth	Mars	
Mean orbital radius	149	227	10^6 km
Eccentricity	0.016	0.093	
Orbital period	365	686	Earth days
Rotational period	24	24.6	hrs
Equatorial radius	6378	3397	km
Mean density	5.51	3.94	g cm^{-3}
Surface gravity	9.78	3.71	m sec^{-2}
Axis tilt	23.45	25.19	degree
Surface temperature	288	230	K
Atmosphere pressure	1013	6	hPa
Solar constant	1370	580	W m^{-2}

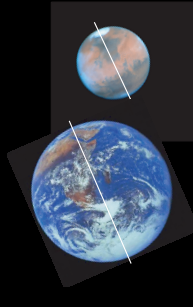
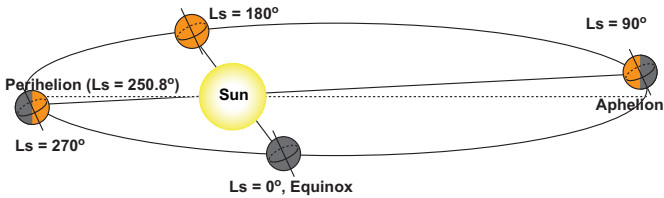



Figure 1.1: The geometry of the revolution of the Mars around the sun during the seasons. The semi major axis is 1.52 (AU). Northern summer corresponds to near the aphelion, and winter is near the perihelion.

Both Martian poles have permanent polar caps that consist of solid carbon dioxide (dry ice) [*Paige et al.*, 1994, *Paige and Keegan*, 1994]. The polar caps show a layered structure where the ice is mixed with a dark colored dust. Carbon dioxide sublimates completely during northern summers, leaving layers of water ice [*Forget et al.*, 1995]. The latitudinal extension of the polar caps depends on seasons, and may accompany by the global atmospheric pressure change of up to 25 %, as measurement on the Viking Lander indicate [*Hourdin et al.*, 1995].

1.3 The Martian Atmosphere

Mars has a very thin atmosphere. It consists mostly of CO_2 (95.3%) [*Conrath et al.*, 1973]. Other important constituents are N_2 (2.7%), Ar (1.6%), a very small amount of O_2 (0.15%) and H_2O (0.03%). The average atmospheric pressure on the ground level of Mars is only about 6 hPa (1% or less of the surface pressure on Earth, or the same pressure as

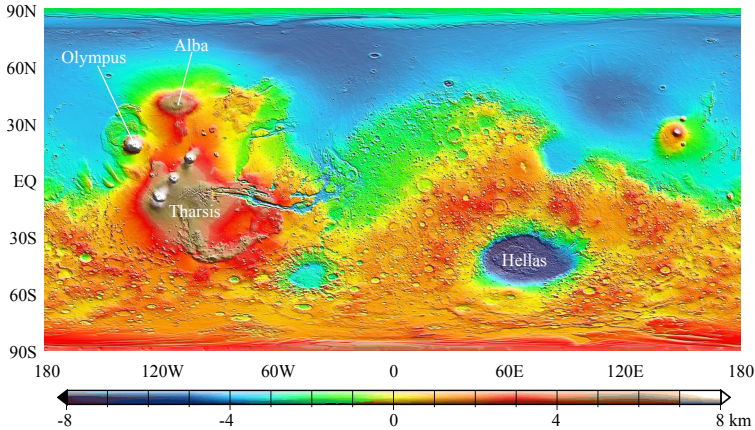


Figure 1.2: The Martian surface map image was taken from the Mars Orbiter Laser Altimeter (MOLA) on board MGS. This first MOLA global topographic model is given by *Smith et al.* [1999].

at about 35 km height). It varies strongly from 9 hPa at the bottom of the deepest basin (Hellas) to 1 hPa at the top of Mt. Olympus. The thin Martian atmosphere maintains the greenhouse effect, but the latter raises atmospheric temperature near the ground by only 5 degrees, far smaller than on Venus and Earth.

Strong seasonal atmospheric pressure variations were measured by the Viking Lander 1 and 2. In particular, the surface pressure peaks during the time between autumnal equinoxes in the Northern hemisphere and winter solstices. The pressure rises slightly also near the aphelion before the summer solstices. The differences in the degree of the atmospheric temperature increase near perihelion and aphelion are related to the eccentricity of the Martian orbit. The meltdown of the dry ice in the Southern polar cap near the perihelion is accompanied by the increase of the atmospheric CO_2 concentration, and, therefore, by the rise of the atmospheric pressure. Afterwards, as the temperature decreases again, CO_2 freezes over, and the atmospheric pressure also gets lower. During aphelion, the rate of CO_2 melting is lower because of the greater distance from the Sun, and the atmospheric pressure increase is weaker compared to perihelion. Diurnal air temperature variations are controlled by the absorption of the solar radiation by the atmospheric CO_2 [Smith et al., 1999]. As the thermal capacity of the air is small, the temperature variations are stronger compared to Earth.

1.4 Atmospheric Waves

The atmospheres are usually subdivided into vertical layers according to the atmospheric temperature distributions. These layers are shown in Figure 1.3 for Mars in comparison

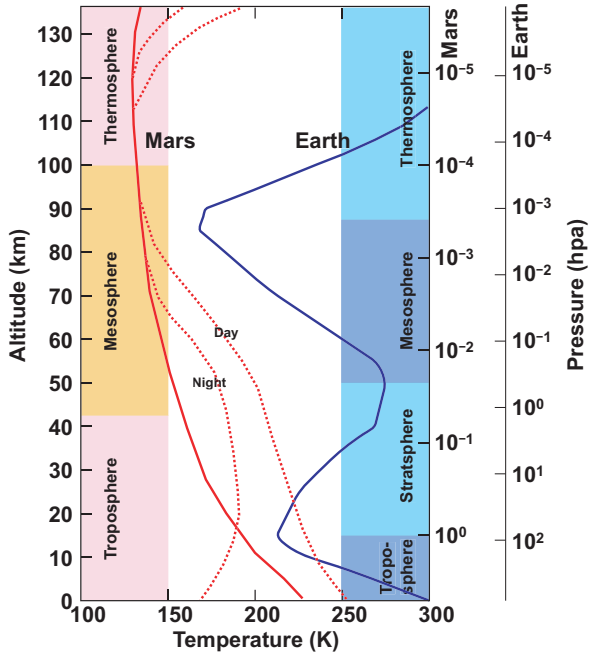


Figure 1.3: The variation of temperature with height in the Mars (Red line) and Earth (blue line) atmosphere. The red solid line is valid in the non dusty season, and the dotted lines correspond to the dusty season during day and night. Boundaries between the major regions of the atmosphere (the lower, the middle and the upper atmosphere) occur at heights of about 40 km and 100 km. Adapted from a temperature profile by Zurek [1992].

to Earth. The lowest level is called troposphere. The atmospheric temperature and circulation in the troposphere is strongly affected by the surface [Haberle, 1999]. In particular, the globally averaged temperature decreases with height in the troposphere because of the influence of the overheated surface. On Mars, the troposphere extends up to 40 km compared to 15 km on Earth. The stratosphere is the layer with the inversed temperature gradient. On Earth, the stratosphere ($\approx 15\text{--}50$ km) is formed due to the existence of the ozonosphere. The ozone strongly absorbs the solar ultra violet radiation and provides a significant heating to the air. On Mars, the amount of the ozone is negligible. Therefore, Mars has no stratosphere. The thermosphere is the upper part of the atmosphere. Temperature grows up with height in the thermosphere due to the strong absorption of the solar EUV and X-rays radiation as well as of high energy cosmic particles. The thermosphere is primarily driven by this solar forcing, and the molecular viscosity is strong enough that it dominates the dynamics there. The thermosphere on Mars begins somewhat higher (≈ 100 km) than that on Earth (≈ 90 km). The areas above the stratosphere (on Earth) and

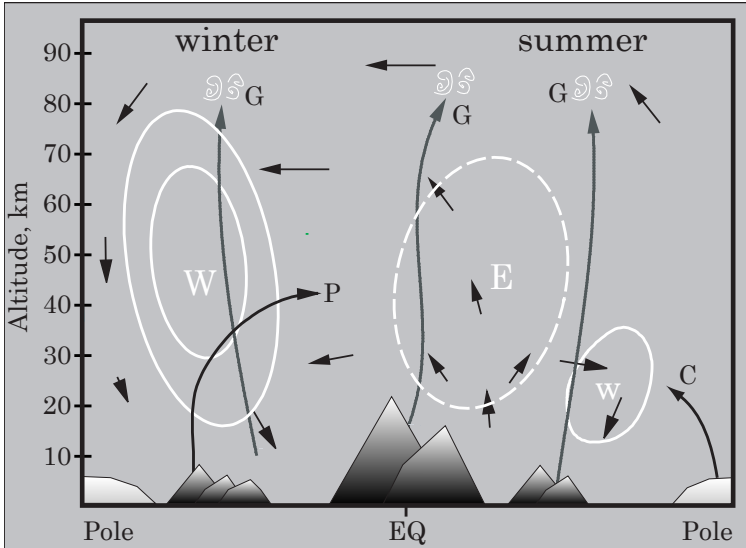


Figure 1.4: The general characteristics of the atmospheric circulation referred to the summer in the Northern hemisphere. In this figure planetary waves P , gravity waves G , condensation flow C , and zonal west wind W and east wind E are emphasized.

the troposphere (on Mars) are called mesosphere. The temperature and circulation in the mesosphere are almost equally determined by the outer forcing (solar radiation absorption), and the mechanical forcing coming from the lower atmosphere. Sometimes, the planetary tropospheres are called the “lower atmospheres”, the upper parts of the thermospheres have the name “upper atmospheres”. The layers between the lower and upper atmospheres are called the “middle atmosphere”. On Earth, the middle atmosphere includes the strato-, meso- and lower thermosphere, whereas on Mars, this term denotes the upper part of the troposphere, mesosphere, and the lower thermosphere.

The vertical coupling between the atmospheric layers on Earth is schematically shown in Figure 1.4. The main agents which provide the momentum, heat and energy exchange in the vertical domain are the atmospheric waves. In the troposphere, the flow over the topography, thermal contrasts over land and oceans, or over land with different thermal characteristics, generate the waves with largest horizontal wavelengths. Since these wavelengths are comparable to the planetary diameter, the waves are called “planetary waves”. Instability of the zonal mean flow generates longitudinal disturbances of somewhat smaller size. These waves with horizontal wavelengths from $1/3$ to $1/10$ of the latitudinal circle are called “synoptic” scale planetary waves. They are seen as a meandering of the mean zonal flow, that consequently develops into cyclones and anticyclones. Since these waves have noticeable horizontal phase velocities (with respect to an observer on the surface), they are sometimes called “traveling” planetary waves. Synoptic scale trav-

eling planetary waves significantly determine the circulation in the troposphere. These waves usually cannot penetrate higher into the stratosphere (on Earth) or mesosphere (on Mars). Instead, large-scale planetary waves can. The latter not only strongly affect the circulation there, but are the major driving force for the global meridional transport in the stratosphere.

The other class of atmospheric waves are the so-called “gravity waves” (GW), or buoyancy waves. They have horizontal wavelengths from several tens to several hundreds of km, periods from about 10 min to several hours (but always less than the rotational period of the planet). They are excited in the lower atmosphere by a variety of sources (like flow over the topography, convection, atmospheric fronts, etc.), and can propagate vertically. The amplitudes of these waves grow with height (due to the density decrease), and at some point the wave breaking occurs. The momentum, heat and energy carried out from denser lower layers is released in the mesosphere and lower thermosphere. Gravity waves are the major driving factor in the mesosphere and lower thermosphere of both Mars and Earth.

The third class of atmospheric waves are the solar tides. Caused by diurnal variations in the solar radiation absorption at or near the surface and in the atmosphere itself, these waves have periods of the forcing (“diurnal tides”) or of higher harmonics (“semi-diurnal tides”, etc.). Solar tides, like planetary and gravity waves, transport the momentum and energy upward, break and/or dissipate, and thus release them in the mesosphere and lower thermosphere. Together with PW and GW, solar tides maintain the meridional circulation in the middle atmosphere.

1.5 Scientific Motivation

Solar tides, planetary and gravity waves play an important role in the global circulation of Mars [Wilson and Hamilton, 1996; Banfield *et al.*, 2000; Banfield *et al.*, 2004]. Since the atmosphere is thin, the disturbances generated near the surface easily transport the momentum and energy upward. The middle atmosphere of Mars is extremely sensitive to the forcing from these atmospheric disturbances. This high sensitivity is probably due to the strong coupling between atmospheric layers through vertically propagating planetary and gravity waves and tides. A large part of the wave action is able to propagate between the hemispheres. Therefore, the knowledge of the middle and upper atmosphere dynamics contributes to a better understanding of the general circulation and climate of Mars.

The rugged Martian topography and the contrasts in the thermal properties of the soil provide an ample source of planetary and gravity waves. The planetary boundary layer is significantly shallower (≈ 200 m) on Mars than on Earth (≈ 3 km). This means that the disturbances excited near the Martian surface experience less damping from the diffusive boundary layer than on Earth. In the terrestrial atmosphere, the major source of solar tides is the diurnal variation in the absorption of the solar radiation by the water vapor in the troposphere. On Mars, most of the absorption comes from the surface. This variations in the heating are transferred to the atmospheric air, and represent the major source of the tides. Recently detailed topography [Delacourt *et al.*, 2003], surface albedo [Christensen *et al.*, 2001], and thermal inertia [Mellon *et al.*, 2000] maps were obtained. These new data facilitated an improvement in numerical simulations with general circulation models

(GCM) to account for more precise representation of the wave generation.

General circulation models are an important and convenient tool in studying atmospheric processes. Martian GCMs are becoming increasingly sophisticated both due to improved parameterizations of physical processes, and due to more data from space missions and ground-based observations. By designing numerical experiments, it is possible to explore the sensitivity of atmospheric parameters to various physical processes and factors.

The purpose of this work is to study the influence of the surface on the Martian atmosphere dynamics, and especially on the global circulation in the middle atmosphere. The main tool used here is the general circulation model of the Martian atmosphere called MAOAM. This model is the result of collaboration between the University of Munich, the Leibniz Institute of Atmospheric Physics and the Max Planck Institute for Solar System Research. It was under development for a number of years. The author took part in this development, in designing and carrying out numerical experiments with the GCM, and in analyzing the results.

The structure of this work is the following. Chapter 2 describes the general circulation model. A full description of this GCM is beyond the scope of this thesis. Only the relevant parts of the model in the development of which the author took part are described. The main results are given in Chapter 3. There, the results of sensitivity runs to explore various aspects of the influence of the surface on the general circulation of Mars are presented. These results contribute to the understanding of the atmospheric dynamics. At the same time, the numerical experiments were a part of the rigorous GCM testing and validation process. Comparisons of the model results with the measurements obtained from the Thermal Emission Spectrometer onboard Mars Global Surveyor (MGS–TES) [Banfield *et al.*, 2000; Smith, 2004] constitute the content of Chapter 4.

2 Model Description

The main goal of the MAOAM project was to develop a general circulation model (GCM) of the Martian atmosphere in the altitude range from the surface to approximately 130 km. The new model is based on the mechanistic Mart-ACC (Martian Atmosphere – Circulation and Climate) model [Ebel and Berger, 1997]. The latter model was developed in the context of the Mars-96 mission. This model was completely redesigned to accommodate for more effective numerical procedures and parallel processing. Significant changes were introduced to its dynamical core, in particular, to the discretization, time integration scheme, horizontal diffusion and near pole filtering. New physical parameterizations have been adapted from terrestrial atmospheric GCMs or newly developed. A detailed description of the MAOAM GCM along with the discussion of its performance is presented in [Hartogh et al., 2005].

Figure 2.1 presents a flowchart of the MAOAM GCM code structure. It consists of four big and interconnected modules. The “driver” module controls the program flow, keeps track of the model time, and controls the multiprocessing, if the parallel computation regime is involved. At first, it initializes all physical constants, parameters, and fields, reads the surface property data (topography, thermal inertia, and surface albedo maps), reads the initial condition data for the field variables in the “restart” regime, or prescribes them in the “spinup” regime. Then the driver controls the time progression of the simulation. The “model” module controls the computations during one time step. In general, this part includes three big steps: calculations of the time derivatives (tendencies) due to the dynamics, due to the subgrid-scale physics, and, finally, finding the field variables at the time $t + \Delta t$. The steps 1 and 3 are coded in the “model” module, while the step 2 is contained in the “physics” part of the code. Calculations of the tendencies due to the “physics” usually consume most of the CPU time in the modern general circulation models. In MAOAM, this part takes up to 95 percent of the total time, depending on the model setup.

Finally, the “diagnostics” module handles the model output. Because the amount of output data is enormous, the diagnostics must be optimized and focused on particular tasks: the appropriate averaging, collecting only necessary data, computation of various diagnostics quantities out of the field variables.

The authors contribution in the development and modifications of the MAOAM model is shown in Figure 2.1 with small stars in the lower right corners of the appropriate boxes. The double bold stars denote the parts which were largely developed by the author. Single bold stars show the parts of the code where the contribution of the author was significant. Finally, single contoured stars mark the parts of the model where the author had to cooperate closely with other model developers in order to incorporate updates.

In this chapter, a brief description of the MAOAM GCM and some physical parame-

Flowchart

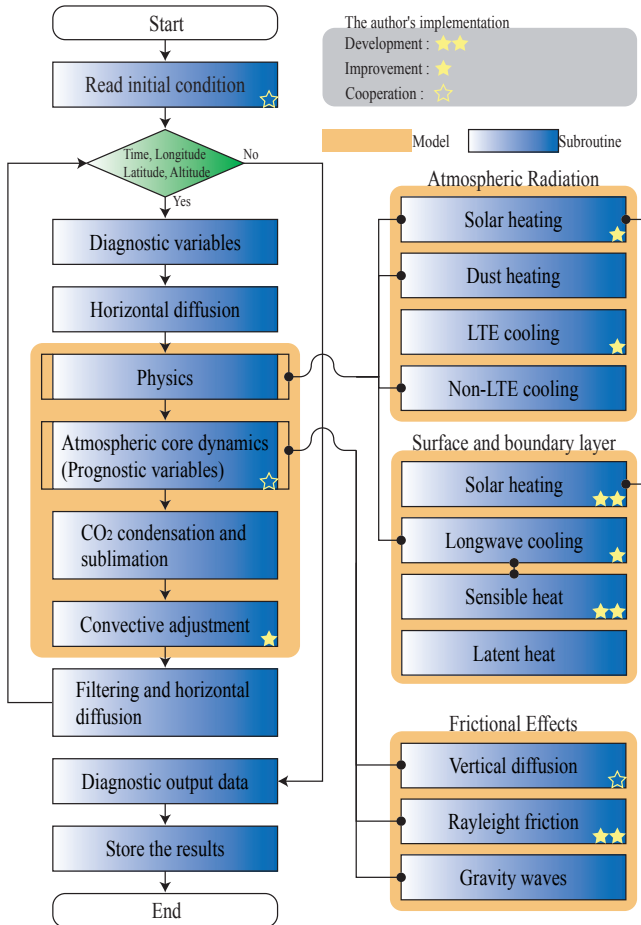


Figure 2.1: A flowchart showing the simulation process with MAOAM. See description in the text. The author's participation is denoted with the stars in the lower right corners of the appropriate boxes. Double bold stars show the parts largely developed by the author. Single bold stars mark the parts of the code where the participation of the author was significant. Single contour stars denote the parts where the author collaborated with other developers.

terizations is presented. These are the parameterizations and the numerical code in which the author was directly involved in developing, programming, implementing, testing and validating. A short description of the model discretization is given at the end of this chapter.

2.1 Basic Equations

In our work, we use the log-pressure vertical coordinate system defined as $z \equiv -H \ln(p/p_s)$, where p_s is a standard reference pressure (taken as 6 hPa) and H is a mean scale height ($\equiv RT_s/g$, T_s is a constant reference temperature, R is the gas constant, and g is the gravity constant). We use $H = 10.3$ km for Mars, corresponding to $T_s \approx 200$ K. In this coordinate system, the atmosphere is always in hydrostatic equilibrium. The horizontal momentum equations, the thermodynamic equation, and the continuity equation may be expressed in spherical coordinates [Holton, 1975; Haberle et al., 1997] as follows

$$\begin{aligned} \frac{\partial u}{\partial t} + \frac{\partial}{\partial x}(u^2) + \frac{1}{\cos\phi} \frac{\partial}{\partial y}(uv\cos\phi) + \frac{1}{\rho} \frac{\partial}{\partial z}(\rho uw) \\ = v \left(f + \frac{u \tan^2 \phi}{a} \right) - \frac{\partial \Phi}{\partial x} + F_M, \end{aligned} \quad (2.1)$$

$$\begin{aligned} \frac{\partial v}{\partial t} + \frac{\partial}{\partial x}(uv) + \frac{1}{\cos\phi} \frac{\partial}{\partial y}(v^2\cos\phi) + \frac{1}{\rho} \frac{\partial}{\partial z}(\rho vw) \\ = -u \left(f + \frac{u \tan^2 \phi}{a} \right) - \frac{\partial \Phi}{\partial y} + F_M, \end{aligned} \quad (2.2)$$

$$\begin{aligned} \frac{\partial T}{\partial t} + \frac{\partial}{\partial x}(Tu) + \frac{1}{\cos\phi} \frac{\partial}{\partial y}(Tv\cos\phi) + \frac{1}{\rho} \frac{\partial}{\partial z}(\rho Tw) \\ = -\frac{\kappa T}{H} w + \frac{Q}{c_p} + F_T, \end{aligned} \quad (2.3)$$

$$\frac{\partial u}{\partial x} + \frac{1}{\cos\phi} \frac{\partial}{\partial y}(v\cos\phi) + \frac{1}{\rho} \frac{\partial}{\partial z}(\rho w) = 0, \quad (2.4)$$

where

$$\frac{\partial}{\partial x} = \frac{1}{a \cos\phi} \frac{\partial}{\partial \lambda}; \quad \frac{\partial}{\partial y} = \frac{1}{a} \frac{\partial}{\partial \phi},$$

where ϕ is latitude, λ longitude, and $a \approx 3394$ km the Martian radius. The primitive equations are frequently written using the temperature T instead of potential temperature, θ , in the following form:

$$\theta = T (p_s/p)^\kappa = T \exp(\kappa z/H), \quad (2.5)$$

where $\kappa = R/c_p$ and c_p is the specific heat at constant pressure. Other variables are the components of the velocity (u, v, w) (positive eastward u , southward v , and upward

w), the atmospheric density ρ , Coriolis parameter $f = 2\Omega\cos\phi$, geopotential Φ , radiative heating Q , and frictional forces $F_{M,T}$.

Under the hydrostatic equilibrium, the vertical pressure gradient balances the gravity force, $dp = -\rho g dz$ which can be rewritten as a function of the geopotential Φ . The difference between the geopotential at the two levels is given by

$$d\Phi = g dz = \frac{R\bar{T}}{H} dz, \quad (2.6)$$

where \bar{T} is the average temperature of the layer.

2.2 Frictional Effects

The friction force can be neglected except close to the planetary surface, and in regions of strong wind shear near jet streams. The eddy friction due to convective mixing and breaking gravity waves may also be important in other parts of the atmosphere.

The friction force, which was symbolically written as $F_M \equiv (F_x, F_y, F_z)$, is equal to the divergence of a stress tensor τ . The zonal (eastward) component of the friction force consist of three parts:

$$F_x = -\frac{1}{\rho} \left(\frac{\partial \tau_{xx}}{\partial x} + \frac{\partial \tau_{yx}}{\partial y} + \frac{\partial \tau_{zx}}{\partial z} \right). \quad (2.7)$$

Near the surface the strongest wind shears are in the vertical direction, so that one can neglect the first two terms in F_x . Thus

$$F_x = -\frac{1}{\rho} \frac{\partial \tau_{zx}}{\partial z}. \quad (2.8)$$

The stress tensor can be written as a time covariance of velocity fluctuations $\tau_{zx} = \overline{\rho w' u'}$, where the bar indicates a time average, and the prime is a departure from the time average. Thus, a flux-gradient relationship (the Newton viscosity law) of momentum and sensible heat are given by

$$\tau_{zx} = \overline{\rho w' u'} = -\rho K_c \frac{\partial u}{\partial z}, \quad (2.9)$$

$$\tau_{z\theta} = \overline{\rho w' \theta'} = -\rho K_c \frac{\partial \theta}{\partial z}, \quad (2.10)$$

where K_c (in $\text{cm}^2 \text{s}^{-1}$) is the coefficient of eddy viscosity (the vertical diffusion coefficient), where the subscript denotes u , v , θ . The tendencies due to turbulent vertical diffusion are calculated as follows:

$$F_x = \frac{1}{\rho} \frac{\partial}{\partial z} \left(\rho K_u \frac{\partial u}{\partial z} \right), \quad (2.11)$$

$$F_y = \frac{1}{\rho} \frac{\partial}{\partial z} \left(\rho K_v \frac{\partial v}{\partial z} \right), \quad (2.12)$$

$$F_T = \frac{1}{\rho} \frac{\partial}{\partial z} \left[\rho K_\theta \left(\frac{\partial T}{\partial z} + \frac{RT}{c_p H} \right) \right]. \quad (2.13)$$

The vertical diffusion coefficients are variable and reflect the intensity of the turbulent mixing. Following *Klemp and Wilhelmson* [1978], and *Forget et al.* [1999], K_c can be determined using

$$K_c = \frac{C_1 E^{\frac{1}{2}} l}{\varphi_c}, \quad (2.14)$$

where E is the turbulent kinetic energy, C_1 is a constant ($=0.516$), l is the mixing length for the statically neutral case, φ_c the static stability functions determined locally by the dimensionless vertical temperature gradient. We use the formula suggested by *Blackadar* [1962] for the mixing length, $l = kz/(1+kz/l_a)$, where the k ($=0.40$) is the von Karman constant, and the asymptotic mixing length l_a is the adjustable parameter that we fixed to a value of 200 m following *Haberle et al.* [1993].

The following stability functions are defined. Their values depend on the sign of the Richardson number Ri . For unstable condition ($Ri < 0$), we chose

$$\varphi_{u,v}^2 = \frac{\varphi_\theta}{C_2} = (1 - 40Ri)^{-\frac{1}{3}}, \quad (2.15)$$

and

$$\varphi_{u,v} = \frac{\varphi_\theta}{C_2} = 1 + 12Ri \quad (2.16)$$

for the stable conditions ($Ri > 0$), where $C_2 = 0.85$ is the constant. Ri is defined as

$$Ri = \frac{g}{\theta} \frac{\partial\theta/\partial z}{\Lambda^2}, \quad (2.17)$$

where $\Lambda = \partial u/\partial z + \partial v/\partial z$ is the wind shear.

The computation of mixing coefficients is based on the equation for the evolution of the turbulent kinetic energy E [*Mailhot and Benoit*, 1982; *Forget et al.*, 1999]:

$$\frac{\partial E}{\partial t} = C_3 E^{1/2} - C_4 E^{3/2} + \frac{\partial}{\partial z} \left(K_c \frac{\partial E}{\partial z} \right) \quad (2.18)$$

where $C_3 = K_{u,v} \Lambda^2 + K_\theta (g/\theta) (\partial\theta/\partial z)$, this term can contribute to the amplification ($C_3 > 0$) or decay ($C_3 < 0$). $C_4 \approx 0.1/l_a$ is always a positive constant.

2.3 The Convective Adjustment

During the model integrations, the vertical temperature gradient may become super-adiabatic. Those situations are especially likely to happen in regions of a strong heating on the surface. To allow for the convective effects in the model, the convective adjustment [*Manabe and Strickler*, 1964; *Ramanathan and Coakley*, 1978] is carried out in the models such that the temperature profile is adjusted to the dry adiabatic one.

The decrease of temperature with increasing altitude is often called the ‘‘lapse rate’’. The adiabatic lapse rate Γ_d can be obtained by differencing the Equation (2.5) and equating $d\theta/dz = 0$

$$\Gamma_d = -\frac{dT}{dz} = -\frac{\kappa T}{p} \frac{dp}{dz} = -\frac{\kappa T \rho}{p} \frac{d\Phi}{dz} = -\frac{g}{c_p}, \quad (2.19)$$

$$\Gamma_d = -\frac{dT}{dz} = -\frac{\kappa T}{p} \frac{dp}{dz} = -\frac{\kappa T}{H}. \quad (2.20)$$

If the potential temperature varies with height, then the actual lapse rate $\Gamma = -dT/dz$ will differ from the dry adiabatic lapse rate Γ_d . In our model we use the Equation (2.20).

Making use of Equation (2.20), the convective condition will be evaluated from equations of the following type:

$$\varphi_s = (\Gamma - \Gamma_d) dz = -dT + \frac{\kappa T}{p} dp, \quad (2.21)$$

where φ_s is called the static stability parameter and is related to $\Gamma - \Gamma_d$. If $\Gamma = \Gamma_d$, then an air parcel adiabatically displaced from its position will tend to remain at its new location, since its temperature will be the same as that of its surroundings. On the other hand, if the atmosphere is static stable $\Gamma < \Gamma_d$ (unstable $\Gamma > \Gamma_d$), then an air parcel adiabatically lifted (lowered) from its equilibrium position will tend to sink (rise) back to its original position [Ramanathan and Coakley, 1978].

Under this condition the temperature of two different layers between the bottom layer z_0 and upper layer z_1 is adjusted as follows:

$$T_{z_0} = \frac{\rho_{z_0} T_{z_0} + \rho_{z_1} (T_{z_1} + \Gamma_d)}{\rho_{z_0} + \rho_{z_1}}, \quad (2.22)$$

$$T_{z_1} = T_{z_0} - \Gamma_d. \quad (2.23)$$

2.4 The Radiation Balance

Diabatic heating in the mesosphere is important both as a driving source for the zonal mean circulation and as a damping mechanism for eddies. At any point in the mesosphere, the net diabatic heating rate $Q = Q_S + Q_L$ (K s^{-1}) represents the difference between the heat input by the absorption of the solar insolation Q_S and the cooling due to the divergence of the infrared emission flux Q_L in Figure 2.2. Consider first the case for which net radiative heating is solely due to the infrared CO_2 band, while solar absorption results from the near-infrared bands.

2.4.1 Longwave Radiation

Carbon dioxide affects the transmission of the longwave radiation within the atmosphere in the 15- μm band [Ramanathan and Cess, 1974; Crisp et al., 1986; Hourdin, 1992]. The rate of temperature change (heating/cooling rate) in the layer is

$$Q_L = -\frac{1}{\rho c_p} \frac{\partial F}{\partial z}, \quad (2.24)$$

where F is the flux (W m^{-2}) of longwave described as below.

We now consider the effects of longwave heating and cooling, allowing for both the downward and upward propagation of the radiation fluxes. It can be shown that the upward thermal irradiance at wavenumber ν and height z is

$$F_\nu^\uparrow(z) = \pi B_\nu(0) \tau_\nu(0, z) T + \pi \int_0^z B_\nu(z') \frac{\partial \tau_\nu(z', z)}{\partial z'} dz'. \quad (2.25)$$

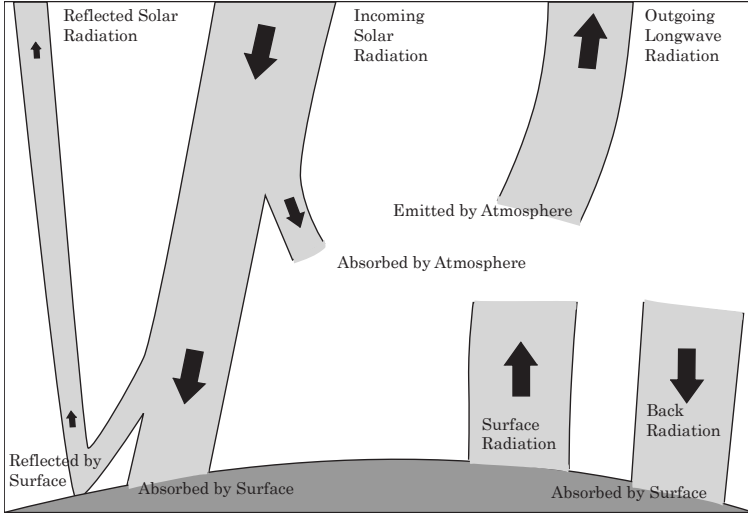


Figure 2.2: The Martian annual and global mean energy balance. Most of the incoming solar radiation is absorbed by the surface. That heat is returned to the atmosphere as sensible heat, as evapotranspiration (latent heat) and as thermal infrared radiation. Most of this radiation is absorbed by the atmosphere, which in turn emits radiation both up and down. The radiation lost to space comes from cloud tops and atmospheric regions much colder than the surface. This causes a greenhouse effect.

Here $\tau_\nu(z', z)$ is the spectral transmittance, averaged over all solid angles to take account of all slanting paths between height z' and z , and $B_\nu(0)$ is the Planck function evaluated at the temperature of the surface. The surface has been assumed to radiate as a black body. Similarly, the downward irradiance is

$$F_\nu^\downarrow(z) = -\pi \int_z^\infty B_\nu(z') \frac{\partial \tau_\nu(z', z)}{\partial z'}; \quad (2.26)$$

there is no boundary term here since the downward thermal irradiance at the top of the atmosphere is zero.

The net long wave spectral irradiance is

$$F_\nu(z) = F_\nu^\uparrow(z) - F_\nu^\downarrow(z) \quad (2.27)$$

and from this net longwave diabatic heating rate Q_L can be calculated using Equation (2.24). Since the resulting expression for Q_L is quite complicated, a useful simplification is the cooling-to-space approximation [Zurek 1985; Andrews, 2000], in which the loss of photon energy to space dominates the other contributions. We obtain a contribution to the

heating rate

$$Q_L = - \sum_{\nu} \frac{\pi B_{\nu}(z)}{\rho c_p} \frac{\partial \tau_{\nu}(z, \infty)}{\partial z} \quad (2.28)$$

The factor π in this equation comes from the integration over all solid angles, and the minus sign is from the fact that the power loss to space implies a negative heating at the height z .

The band absorptance is defined as

$$A(p, T) = \int_{-\infty}^{\infty} a_{\nu}(p, T) d\nu \quad (2.29)$$

where p, T are the total pressure and absolute temperature, a_{ν} is the monochromatic absorption at the wave number ν . In terms of the ratios of the absorbed and transmitted radiation, we may write

$$1 = a_{\nu} + \tau_{\nu}. \quad (2.30)$$

Wide band models generally provide a value of the absorptance A for a whole band as a function of the optical path u . The band models approximate the structure of the CO₂ 15- μm band, these methods are interpolation formulas that connect the observed linear, square root, and logarithmic region of the curve of growth. Such methods have been widely used in studies of atmospheric radiative transfer [Goody and Belton, 1967; Cess and Ramanathan, 1972; Kiehl and Ramanathan, 1983]. They usually assume a simple logarithmic functional form:

$$A(p, T) = 2A_0 \ln \left(1 + u(p) \left[4 + u(p) \left(1 + \frac{1}{\beta(T)} \right) \right]^{-1/2} \right). \quad (2.31)$$

where

$$u(p_{z_1, z_2}) = \frac{Sw}{A_0} = \int_{z_1}^{z_2} \frac{S}{A_0} \left(\frac{p}{1013} \right) dz, \quad (2.32)$$

and

$$\beta(T) = \frac{4\gamma_L}{d} \left(\frac{p}{1013} \right) \sqrt{\frac{2773}{T}} \quad (2.33)$$

are a dimensionless path length and a mean line width parameter, respectively, and $A_0 = 21.3(T/273)^{1/2}$ is the effective band width (cm^{-1}), $S = \delta\nu \sum s_{\nu} = 194.0$ is the band strength ($\text{cm}^{-2} \text{atm}^{-1}$) [Dickinson, 1972], $d = 1.56$ is the mean line spacing (cm^{-1}), $\gamma_L = 0.0064$ is the mean line width (cm^{-1}), w is the absorber amount (optical path, [atm cm]). Then, we can replace the Equation (2.28) as follows:

$$Q_L = \frac{\pi B_{\nu}(z)}{\rho c_p} \frac{\partial A(z, \infty)}{\partial z} = \frac{\pi B_{\nu}(z)}{\rho c_p} \frac{du(p, \infty)}{dz} \frac{dA(u)}{du}. \quad (2.34)$$

2.4.2 Solar Radiation

Atmospheric heating due to absorption of solar radiation in the near-IR bands of CO₂ is negligible below 30 km but becomes considerable above 50 km. A simple parameterization has been included which is similar in its effect to heating rates obtained in radiative transfer in line-by-line calculations performed by *López-Puertas* [1995] and *López-Valverde et al.* [1998] which include non local thermodynamic equilibrium (non-LTE) effects. At pressure $p_0 = 700$ Pa and for a mean Mars–Sun distance $r_m = 227.92 \times 10^9$ m, the heating rate corresponding to a zero solar zenith angle ($\mu = 0$) is taken to be $\partial T/\partial t = 1.3 \text{ K day}^{-1}$ [*Forget et al.*, 1999]. The heating rate at other pressure p , Mars–Sun distance r , and zenith angle μ is then computed as follow:

$$Q_S = 1.3 \frac{r_m^2}{r^2} \sqrt{\frac{p_0}{p}} \tilde{\mu} \left[1 + \left(\frac{p_{nlte}}{p} \right)^b \right], \quad (2.35)$$

where $p_{nlte} = 0.00016$ Pa is the pressure below which non-LTE effects are significant and $\tilde{\mu} = [(1224\mu^2 + 1)/1225]^{1/2}$ the cosine of the solar zenith angle corrected for atmospheric refraction, $b = 1.6$ the pressure scale factor [*Villanueva*, 2004].

2.4.3 Energy Budget at the Surface

For the computation of the surface temperature T_g , a slab model is applied [*Gierasch and Goody*, 1968; *Zhang et al.*, 1982] in the form of the energy budget equation

$$\frac{dT_g}{dt} = \frac{1}{c_g} (F_{Rad} - F_{SH}) - F_G. \quad (2.36)$$

The surface balance considers the net flux of radiation at the surface F_{Rad} , the sensible heat flux into the atmosphere F_{SH} , the heat flow into the substrate F_G in Figure 2.3, and the thermal capacity c_g of the slab defined by the thermal inertia

$$I = \sqrt{k\rho c_p} \quad (2.37)$$

in $\text{J m}^{-2} \text{K}^{-1} \text{s}^{-1/2}$, where k is the thermal conductivity ($\text{W m}^{-1} \text{K}^{-1}$), ρ the soil density (kg m^{-3}) and c_p the specific heat of the soil ($\text{J kg}^{-1} \text{K}^{-1}$). In this model the latent heat flux F_{LH} is neglected.

Blackadar [1979] shows that the following formulation relates the amplitude and phase of the slab temperature, with c_g related to the diurnal frequency ω by

$$c_g = \sqrt{\frac{k\rho c_p}{2\omega}} = I \sqrt{\frac{1}{2\omega}}. \quad (2.38)$$

The net flux of radiation at the surface results from a balance between the solar and surface radiation fluxes:

$$F_{Rad} = F_{SW}^\downarrow - F_{SW}^\uparrow + F_{LW}^\downarrow - F_{LW}^\uparrow, \quad (2.39)$$

where the downward and upward arrows denote the incoming and outgoing radiation components, respectively.

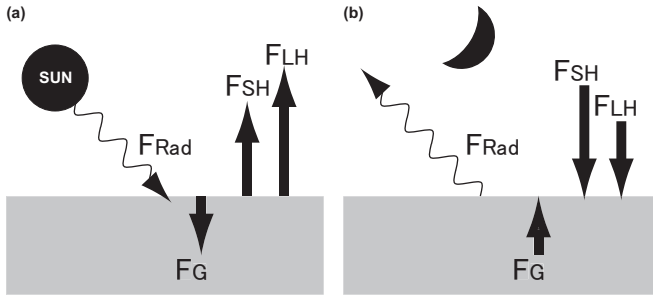


Figure 2.3: Typical variation of terms of the surface energy balance for (a) daytime over land; (b) nighttime over land [Stull, 1997]. The arrow size indicates relative magnitude. All symbols are related to Equation (2.36). F_{LH} denotes the latent heat flux which is ignored in our model.

The incident solar radiation flux is written as

$$F_{SW}^{\downarrow} = (r_{\odot}/r)^2 \sigma T_{\odot}^4 \mu, \quad (2.40)$$

where r_{\odot} is the radius of Sun, r the Mars–Sun distance, σ the Stefan-Boltzmann constant, T_{\odot} the blackbody temperature of Sun and μ the cosine of the solar zenith angle. The outgoing short-wave solar radiation is the part reflected by the surface $F_{SW}^{\uparrow} = A F_{SW}^{\downarrow}$, where A is the surface albedo so that the net short-wave radiation is $F_{SW} = (1 - A) F_{SW}^{\downarrow}$.

The incoming longwave radiation F_{LW}^{\downarrow} which comes from the atmosphere and the outgoing longwave radiation F_{LW}^{\uparrow} are given by the Stefan-Boltzmann law, assuming a given emissivity ϵ [Sutherland et al., 1979; Pollack et al., 1993]. Subscript g and atm denote surface and atmosphere, respectively. The net radiation flux at the surface is then given by

$$F_{Rad} = F_{SW}^{\downarrow} (1 - A) - \epsilon_g \sigma T_g^4 + \epsilon_{atm} \sigma T_{atm}^4, \quad (2.41)$$

The heat fluxes into the ground is calculated from the equation

$$F_G = K_m (T_g - T_m), \quad (2.42)$$

where $K_m \approx \omega$ is the heat transfer coefficient and T_m is set equal to the running zonal average of T_g [Pollack et al., 1981].

The sensible heat flux between two plates due to the combined molecular conduction and turbulent transfer, derived theoretically by Gierasch and Goody [1968], can be written

$$F_{SH} = 0.089 \rho c_p 2^{4/3} \kappa (T_g - T_{atm})^{4/3} \left(\frac{g}{T_{atm} \kappa \nu} \right)^{1/3}, \quad (2.43)$$

where $\kappa \approx 8 \text{ cm}^2 \text{ s}^{-1}$ is the thermal diffusivity, and $\nu \approx 10 \text{ cm}^2 \text{ s}^{-1}$ the kinematical viscosity.

The condensation temperature of CO_2 is approximated as 149.2 K. We use the surface thermal inertia map [Forget et al., 2001] and the surface albedo global map [Christensen et al., 2001] as measured by Mars Global Surveyor–TES.

2.5 Discretization and Parameterization

The spatial discretization of all variables is done in a spherical coordinate system on a regular grid with the resolution Δx , Δy , and Δz in the vertical domain. The derivatives of the field variables $F(t)$ (atmospheric and surface temperatures, three components of the wind velocity, and the geopotential) are approximated with central differences, e.g.

$$\frac{dF(x)}{dx} = \frac{F(x+1) - F(x-1)}{2\Delta x}. \quad (2.44)$$

To prevent a build-up of the kinetic and potential energy at the shortest resolved spatial scales and the associated instability, a horizontal dissipation is introduced in the form of the Shapiro filter (see the flow chart in Figure 2.1). Effectively, the Shapiro filter approximates the scale selective horizontal diffusion acting on the smallest scale disturbances, and not affecting the larger scales.

The temporal discretization is done through the introduction of three time levels for all the variables: the “past”, “now”, and “future”. The time stepping is done using the leapfrog scheme with the time resolution $\Delta t = 100$ s. In the leapfrog method, the “future” values, $F(t + \Delta t)$ are calculated from the “past” $F(t - \Delta t)$ using the time derivatives (“tendencies”) from the “present”, $dF(t)/dt$:

$$F(t + \Delta t) = 2\Delta t \frac{dF(t)}{dt} + F(t - \Delta t). \quad (2.45)$$

Although this scheme gives a second order of the approximation for dF/dt with respect to the finite time step Δt , an instability may develop due to a decoupling the solutions at the odd and even time steps (a zig-zag solution). To avoid this, either the Euler backward schemes ($F(t) = F(t - \Delta t) + (\Delta t)[dF(t)/dt]$) are turned on after a certain amount of time steps [Ebel and Berger, 1987], or the small Asselin time filter (a correction of $F(t)$ after $F(t + \Delta t)$ is calculated) is used [Hartogh *et al.*, 2005].

3 Simulation Results

We carried out numerical sensitivity tests to study the interactions between the Martian atmosphere and the surface. The major mechanism which provides the coupling between the surface and the upper atmosphere are atmospheric eddies. In this work we consider large scale eddies simulated with the model: solar tides and planetary waves. In numerical simulations, it is possible to test hypothetical cases which never occur in reality. These numerical tests help to explain interactions between different physical processes, and to highlight the importance and effectiveness of these processes.

Four main experiments are discussed in the next three sections. They are summarized in Table 3.1: (1) only solar tides are included, but the topography and material distributions on the surface (albedo and the thermal inertia) are neglected; (2) flat topography, but taking account of diurnal variations; (3) only the topography is included, diurnal variations and the surface material distributions are neglected; (4) considering all the physics, i.e. diurnal variations, topography, and the surface albedo and thermal inertia.

The results of simulations confirmed that the interactions between the eddies and the surface take place in the lower as well as in the middle and upper parts of the atmosphere. The global atmospheric circulation in the mesosphere is driven by breaking tides, planetary and gravity waves generated at and near the surface. In this chapter, we focused our analysis on the following: effects of solar tides, thermally and mechanically excited stationary waves, baroclinic waves; effects of the topography and the material properties (albedo and thermal inertia) on the circulation in the atmosphere.

Generally, all the field variables $\psi = u, v, w, T$, etc. can be represented as a sum of harmonics

$$\psi(\lambda, \phi, z, t) = \Psi_{\sigma,s}(\phi, z) \exp \left[-i(\sigma\Omega t - s\lambda + \Theta_{\sigma,s}) \right], \quad (3.1)$$

where Θ is the phase, and the summation is assumed over natural σ and s . Of course, only real parts are assumed in (3.1) for physical variables.

Table 3.1: Numerical sensitivity tests for Section 3.1–3.4.

Run No.	Solar cycle	Topography	Albedo and Thermal inertia
1	+	—	—
2	+	—	+
3	—	+	—
4	+	+	+

3.1 Solar Tides

Solar tides are the longitudinal disturbances which follow the sun and are generated due to the absorption of the solar radiation by the atmosphere and surface. Therefore, sources of the solar tides lie mainly in the middle atmosphere and near the surface.

Figure 3.1 presents the results of the simulation (Run-1) with only diurnal variations of the solar radiation included. This means that only solar tides are allowed to be excited in the model. The arrows in Figure 3.1a show the direction of the wave action flux associated with tides, or the Eliassen-Palm (EP) flux. These arrows indicate that the diurnal disturbances are generated mostly near the surface, and propagate upward. Only the fluxes with the magnitude exceeding a certain value are plotted in Figure 3.1b. It is seen that the magnitude of the wave action flux decreases with height up to 60 km. This suggests that the excitation of the tide near the surface is stronger than in the middle atmosphere. In the Martian atmosphere, the solar radiation is mainly absorbed by CO_2 . This is because the main radiatively active constituent is CO_2 , and no other molecules (like ozone, water vapor, etc) play a noticeable role, unlike in the Earth atmosphere.

The EP flux decreases with height because the tides experience dissipation and/or breaking in the upper atmosphere. Formally this is represented through the divergence or convergence of EP fluxes, $\nabla \cdot \mathbf{F}$. Areas of $\nabla \cdot \mathbf{F} < 0$ are shaded in Figure 3.1a,b. The EP flux divergence enters the equation for the mean zonal circulation [Andrews *et al.*, 1987]:

$$\begin{aligned} \bar{u}_t + \bar{v}^*[(a \cos \phi)^{-1}(\bar{u} \cos \phi)_\phi - f] + \bar{w}^* \bar{u}_z \\ = (\rho_0 a \cos \phi)^{-1} \nabla \cdot \mathbf{F}. \end{aligned} \quad (3.2)$$

where, \bar{v}^* and \bar{w}^* are the residual velocities defined as $\bar{v}^* = \bar{v} - \rho_0^{-1}(\rho_0 \overline{v'\theta'}/\bar{\theta}_z)_z$ and $\bar{w}^* = \bar{w} + (a \cos \phi)^{-1}(\cos \phi \overline{v'\theta'}/\bar{\theta}_z)_\phi$; ϕ is the latitude, f is the Coriolis parameter, and \mathbf{F} is the EP flux. It is seen from (3.2), that $\nabla \cdot \mathbf{F}$ can accelerate or decelerate the mean zonal wind \bar{u} , or force the mean meridional transport \bar{v} .

The analysis of the output from Run-1 shows that the wave action flux is composed of two types of waves. One with the frequency $\sigma = 1$ (diurnal tide), and the other $\sigma = 2$ (semidiurnal tide). They originate from the diurnal variations in heating at the surface and in the atmosphere. The semidiurnal tide represents a second harmonics of the diurnal heating cycle due to the nonlinearity of the atmosphere. It is seen from Figure 3.2 that the semidiurnal $\sigma = 2$ tide dominates above 60 km, except in the Northern polar latitudes higher than 60°N . The $\sigma = 2$ tide is strong in the upper Southern hemisphere, while the $\sigma = 1$ tide dominates in the upper Northern hemisphere. This is caused by the different propagation properties for both tidal components.

The tidal energy flux directed, in general, upward from the surface and the middle atmosphere (where tides are excited). A significant propagation in the meridional direction is also seen in Figure 3.1a. Thus, tides are spread into all areas of the atmosphere. According to the EP flux divergence in Figure 3.1b, most of the energy flux dissipates in the upper atmosphere. There, it strongly affects the mean circulation because the atmospheric density gets lower with height. The negative EP flux divergence is in the winter hemisphere and in the polar region of the summer hemisphere, but is positive in the summer middle hemisphere. The areas of the positive EP flux divergence is denoted by the light shade in Figure 3.1b. It shows that the associated torque applied on the zonal wind is eastward. On the other hand, the negative EP flux divergence means the westward zonal

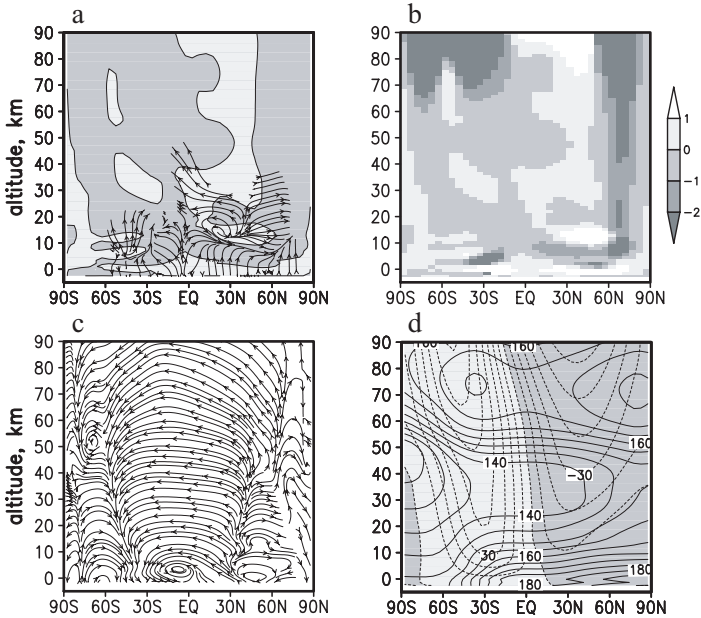


Figure 3.1: Results of the run including only tides (Run-1) for perpetual $L_s = 90^\circ$ after 40 sols spinup. (a): The arrows denote the EP flux, and the negative EP flux divergence shaded. (b): EP flux divergence for in $[m s^{-1} sol^{-1}]$. (c): Stream lines are for the residual mean zonal circulation. (d): Solid lines are for the zonal mean temperature with the contour interval 5 K, dotted lines on the shade denote westward (negative) zonal mean winds, and the dotted lines on the light shade is for eastward (positive) zonal mean winds with the contour interval $10 m s^{-1}$.

acceleration of the mean zonal wind \bar{u} , as follows from the simplified version of Equation (3.2) (see [Andrews *et al.*, 1987])

$$\bar{u}_t - f_0 \bar{v}^* = \rho_0^{-1} \nabla \cdot \mathbf{F}. \quad (3.3)$$

Figure 3.1c shows that a large southward meridional circulation exists between the upwelling in the summer hemisphere and the downwelling in the winter hemisphere. It is also caused by the EP flux divergence, as seen from the equation above. In general, the Coriolis force associated with the factor f causes the flow to curve toward the right hand side in the Northern hemisphere, and towards the left hand side in the Southern hemisphere. To balance the torque by the flux divergence with the Coriolis force for the flows, the meridional flow must appear. Therefore, the meridional circulation is caused by the EP flux divergence.

The upper atmospheric temperature has two warm spots in the both hemispheres, as

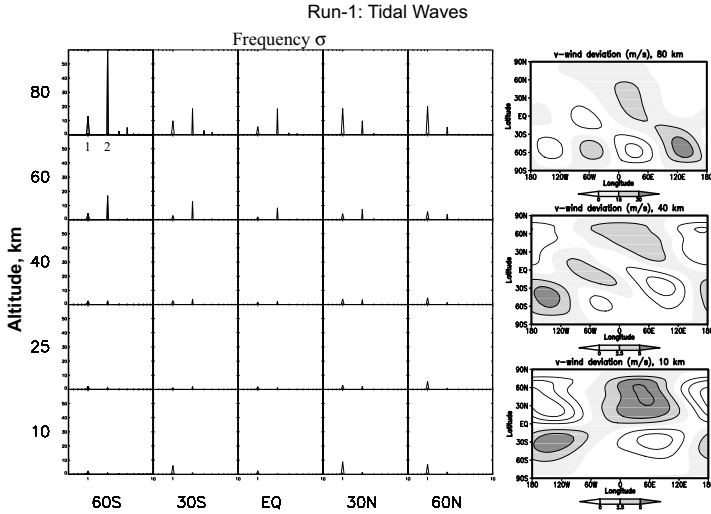


Figure 3.2: Amplitude of the v -wind deviation ($v - \bar{v}^t$) vs. σ in Run-1. A 40 sols time series has been analyzed. Panels on the right sides are also v -wind deviations in latitude-longitude projection at 10 km (bottom), 40 km (middle) and 80 km (top). Contour intervals are 2.5 m s^{-1} (middle and bottom) and 15 m s^{-1} (top).

shown in Figure 3.1d. Although the solar radiative heating is stronger in the summer hemisphere above the middle atmosphere, the cooling occurs over 70 km because the upwelling flow creates an adiabatic expansion of the air, and therefore, the cooling in the summer polar region. Hence, the temperature distribution over the summer pole is determined by the balance between the adiabatic cooling and solar heating. In the winter hemisphere, an unusual thing is that the warm spot exists at 75 km at 30°S because the adiabatic heating exceeds the diabatic one by about 8 K Day^{-1} .

The energy of waves modifies the residual circulation, changes the temperature distribution, and drives the thermal wind. These effects are known as the “wave-driven circulation”.

3.2 Thermally Forced Stationary Planetary Waves

The surface temperature depends on the thermal inertia and surface albedo for a given solar and thermal radiative fluxes. The thermal radiation exchange is faster if the thermal inertia is small. Then the temperature difference is larger during days and nights (see Equation (2.36–2.38)). For example, the thermal inertia for snow and dry soil is of the order of $10^2 \text{ J m}^{-2} \text{ s}^{1/2} \text{ K}^{-1}$, for the saturated soil, still water and ice it is of the order of 10^3 , and 10^4 for stirred water. In the areas with large thermal inertia, the surface

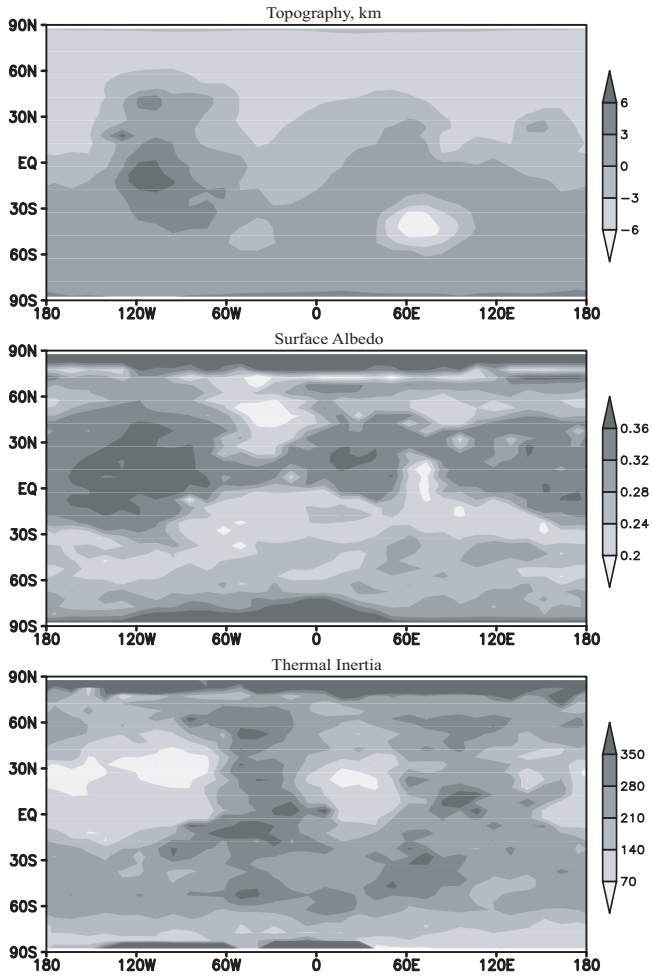


Figure 3.3: These surface parameters are used in the model. Top: Martian topography in km; middle: the surface albedo map; and bottom: the thermal inertia map in $\text{J m}^{-2} \text{s}^{1/2} \text{K}^{-1}$. Note that the permanent ice caps on both poles (e.g. north and south of 120°W to 0°) play an important role in the stationary wave generation in the polar region.

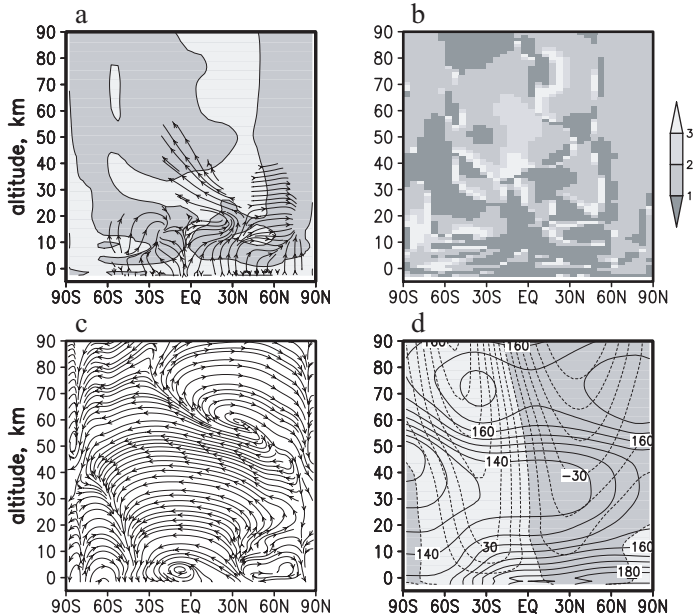


Figure 3.4: Panels (a, c, d) are the same as in Figure 3.1, but for Run-2. Panel (b) shows the ratio of the EP flux divergence (Run-2 divided by Run-1), which means that in the lightest area the EP flux divergence is increased in Run-2.

temperature keeps warm even during the night, the same happens for the terrestrial oceans [Ringler and Cook, 1999].

The Martian surface has a significant contrast of the thermal inertia and the surface albedo, as shown in Figure 3.3 [Kieffer *et al.*, 1997]. The thermal inertia alternates from $I = 80$ to 300, and creates a net contrast in the middle latitudes between 15°S and 50°N . One can expect to find stationary waves generated over the uneven surface material characteristic, like over the oceans and land contrasts on Earth. The numerical experiment Run-2 is effectively the same as Run-1 but the thermal inertia and surface albedo maps were added. The topography is flat in this experiment so far.

In Figure 3.4a, although the EP flux distribution is similar to the one in Figure 3.1a, the residual circulations are different, especially above the middle atmosphere around 50 km in Figure 3.1c and 3.4c. The meridional circulation in the northern upper atmosphere turns into the opposite side above the equator and is directed towards the summer polar region despite the positive EP flux divergence which provides the torque towards the equator. The summer polar warm spot is not only smaller than in the previous simulation in spite of the adiabatic heating caused by descending flow, but also the winter hemisphere's warm spot is stronger although the downward flow is almost half of the intensity compared to

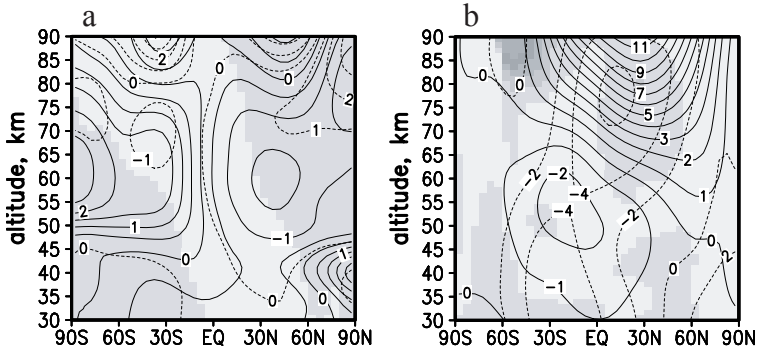


Figure 3.5: These figures compare the results of Figure 3.1 and 3.4 in the middle atmosphere to show differences in detail. (a): Solid lines are for the averaged temperature deviation ($\overline{T}_{Run2}^x - \overline{T}_{Run1}^x$), dotted are for the cooling rates deviation, and the shaded area denote the negative w-winds deviations (downflows). (b): Solid lines are for the v-winds deviations, dotted are for the u-winds deviations, and shade is for the EP flux divergence differences.

the previous simulation.

Some stationary waves are present in the simulation in the middle atmosphere. They are generated over surface contrasts of the albedo and thermal inertia, and propagate according to the EP flux in Figure 3.4a. These waves have magnitudes of $10\text{--}20\text{ m s}^{-1}$, longitude wavenumbers $s = 1$ and 2 , and are distributed symmetrically around the equator in Figure 3.6. The magnitudes usually increase with height, as mentioned in the previous Section 3.1, until the waves are completely obliterated. The inhomogeneous surface features modulate tidal waves as well. The latter shows up in the amplitude of the solar tide $\sigma = 1$. Compared to the Run-1 it becomes stronger in the upper Southern hemisphere, and weaker in the Northern hemisphere in Figure 3.7.

In the upper Southern hemisphere, the positive EP flux divergence forces the equatorward meridional flow, as shown in Figure 3.4b and 3.5b. Therefore, the meridional circulation weakens (compared to Run-1 in Figure 3.5b), as does its descending branch. The corresponding adiabatic cooling is then weak, causing weaker polar warming in Figure 3.5a.

In the upper atmosphere near the equator, with this positive flux divergence scenario and small Coriolis force, an air parcel stands still when the meridional transport in the Southern hemisphere slows down, and turns to the north.

In the upper Northern hemisphere, the warm area over the polar region is colder than in Run-1. This is because in order to compensate for the adiabatic heating by the descending flow, the atmospheric cooling due to the CO_2 increases. On the other hand, the descending flow converges over the north pole and produces the adiabatic heating at 40 km in Figure 3.5a, thus inducing the clockwise circulation in the Northern hemisphere.

Figure 3.5a indicates that the difference in temperatures between the Run-1 and Run-

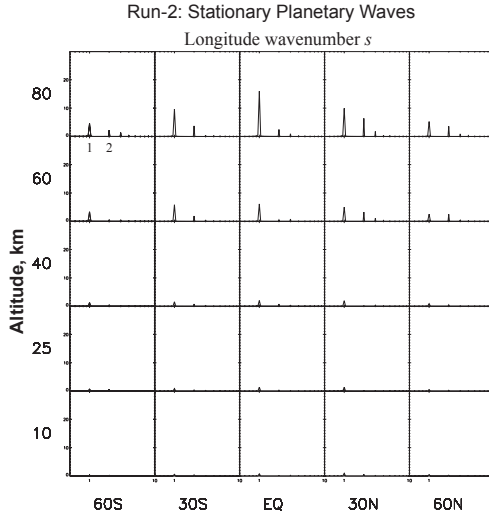


Figure 3.6: Amplitude of v-wind deviation ($v - \bar{v}^x$) for stationary planetary waves in Run-2 from 40 sols of integration at $L_s = 90^\circ$.

2 does not apparently agree with the corresponding cooling rates. The explanation can be given to this: the thermally forced stationary waves modify the meridional flow, and indirectly affect the atmospheric radiative cooling through the modified temperature distribution.

Therefore, the upper atmospheric circulation is obviously affected by thermally forced stationary waves generated by biases in the solar radiation absorption on the surface associated with spatially varying albedo and thermal inertia.

3.3 Mechanically Forced Stationary Planetary Waves

We use the term “mechanically forced” for the waves which are generated by the flow over the topography.

In the Run-3, the realistic topography was introduced, but the diurnal variations of the solar heating were turned off, and the surface albedo and thermal inertia were set to a constant. As the result, only longitudinal disturbances which appear in the simulation are “mechanically forced” planetary waves. They include forced waves (stationary planetary waves) and free Rossby waves (traveling mid-latitudes waves with non-zero frequencies). Figures 3.8 and 3.9 present the results of the simulation for the Run-3. Figure 3.8 shows the stationary waves with the magnitude of the meridional velocity fluctuations, v' , of about 30 m s^{-1} and the longitude wavenumber $s = 1$. But free Rossby waves with the amplitude of few m s^{-1} and $\sigma < 0$ are too small to be in the simulation. Both appear

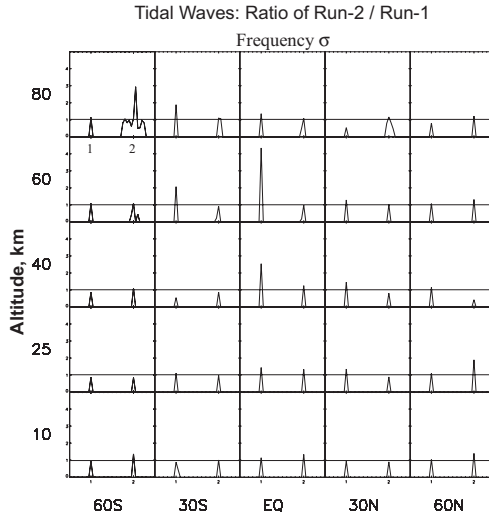


Figure 3.7: Same as in Figure 3.2, but for the ratio of Run-2 and Run-1 for tides ($v - \bar{v}^t$). Frequency $\sigma = 1$ in the equatorial middle atmosphere and $\sigma = 2$ in the southern upper atmosphere have more than 1 m s^{-1} amplitude. This means that the tides are affected by the surface thermal inertia and albedo distributions.

in the winter hemisphere because Rossby waves tend to propagate only into the eastward zonal winds, as the waves with long wavelengths are easily affected by the variation of the Coriolis force f with latitude, the so-called β effect ($\beta = df/dy$, see also *Holton [1992]*). Therefore, the wave action (EP) flux is seen in the areas covered by the eastward jet in Figure 3.9a,d. According to Figure 3.9b, the EP fluxes associated with these waves are about 10 times stronger in the lower atmosphere than those associated with the solar tides.

In Figure 3.9a, the negative EP flux divergence due to the waves generated by the topography dominates strongly in the middle atmosphere in the southern mid-latitudes. The southward torque due to the negative flux divergence forces the meridional wind. This results in the eastward Coriolis force in the Southern hemisphere. The magnitude of the EP flux divergence is the strongest over 30°S at 40 km. The intensified southward transport extends far to the South pole in the middle atmosphere in Figure 3.9c. Accordingly, the downward branch of the circulation cell is also stronger, and the atmosphere is heated up near the poles due to the adiabatic heating. The intensity of the eastward zonal jet is consistent with the strong temperature gradient in this region [*Barnes and Haberle, 1996*]. Consequently, the axis of the jet on the latitude-altitude plane is tilted. In the summer hemisphere around 60°N at 30 km, the northward torque by the negative EP flux divergence creates the clockwise meridional circulation in Figure 3.9c.

Figure 3.9d demonstrates that removal of the solar tide and leaving the topographically generated waves creates a pole-to-pole layer of the temperature maximum at 80 km. This

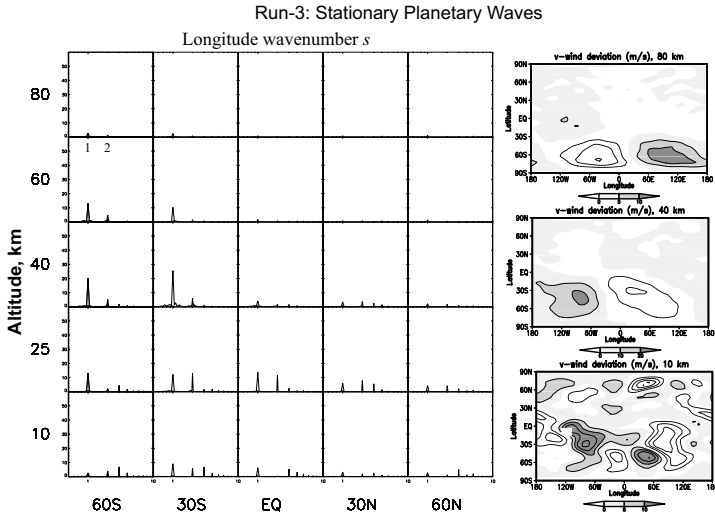


Figure 3.8: Same as in Figure 3.2, but for stationary waves ($v - \bar{v}^x$) in Run-3 (only mechanical forcing is included).

maximum at 80 km reminds of the stratopause in the atmosphere of Earth. However, unlike on Earth where the stratopause is the result of an enhanced solar absorption by ozone and the related diabatic heating, the temperature inversion in the presented run has a pure dynamical reason. Since the heating rates in this run are equal to diurnally averaged heating rates from the control run, all changes in the mean circulation pattern can be attributed entirely to the lack of the forcing by tides.

Stationary planetary waves not only affect the mean zonal circulation but modulate solar tides (Example of Earth reported by *Ringler and Cook* [1999]). The stationary planetary waves influences the solar tides. Figure 3.10 compares the time series of the meridional velocity, v , at 80 km for the Run-4 with the “full physics” included (panel a), and for the Run-2 with the same physics but flat surface (panel b). In both cases, diurnal and semidiurnal tidal signatures are seen. However, the magnitudes of tidal oscillations and their modulation in the absence of stationary planetary waves (panel b) are much weaker. Interactions between the stationary planetary waves and solar tides can occur either directly through nonlinear interactions and/or linear modulation, or by means of changing the background zonal mean circulation, and, therefore, affecting the propagation of both types of eddies.

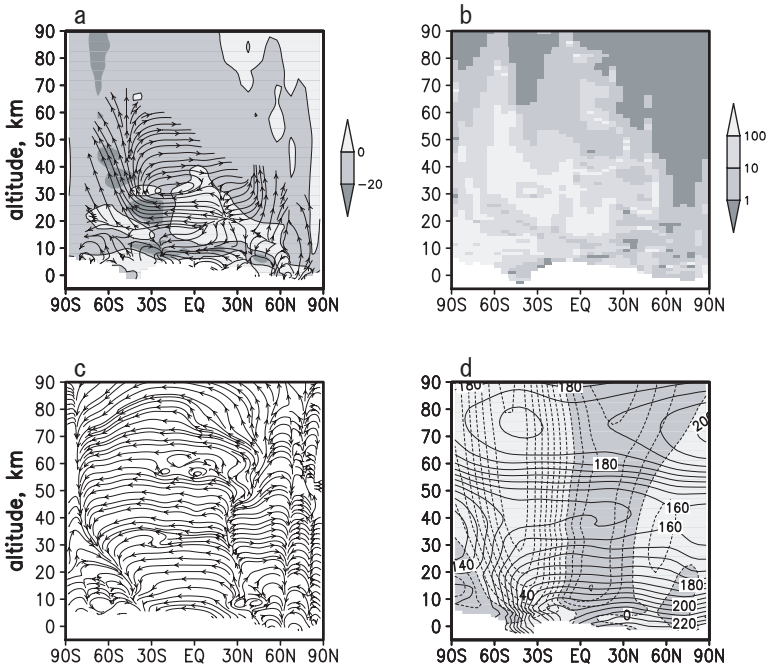


Figure 3.9: Panels (a, c, d) are the same as in Figure 3.1, but for Run-3. (b) is the ratio of the EP flux divergence (Run-3 divided by Run-1), which means that in the lightest area, the EP flux divergence is increased in Run-3 (including only the topography).

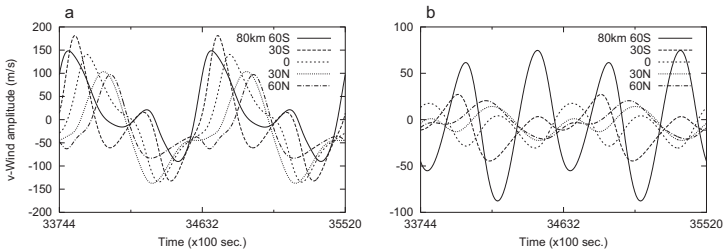


Figure 3.10: Wave oscillations of the local v -wind at 80 km in $L_s = 90^\circ$ (2 sols are shown) after 38 sols running, (a) in Run-4 and (b) in Run-3. According to the figure, the difference in waves shows the influence of stationary planetary waves on solar tides.

3 Simulation Results

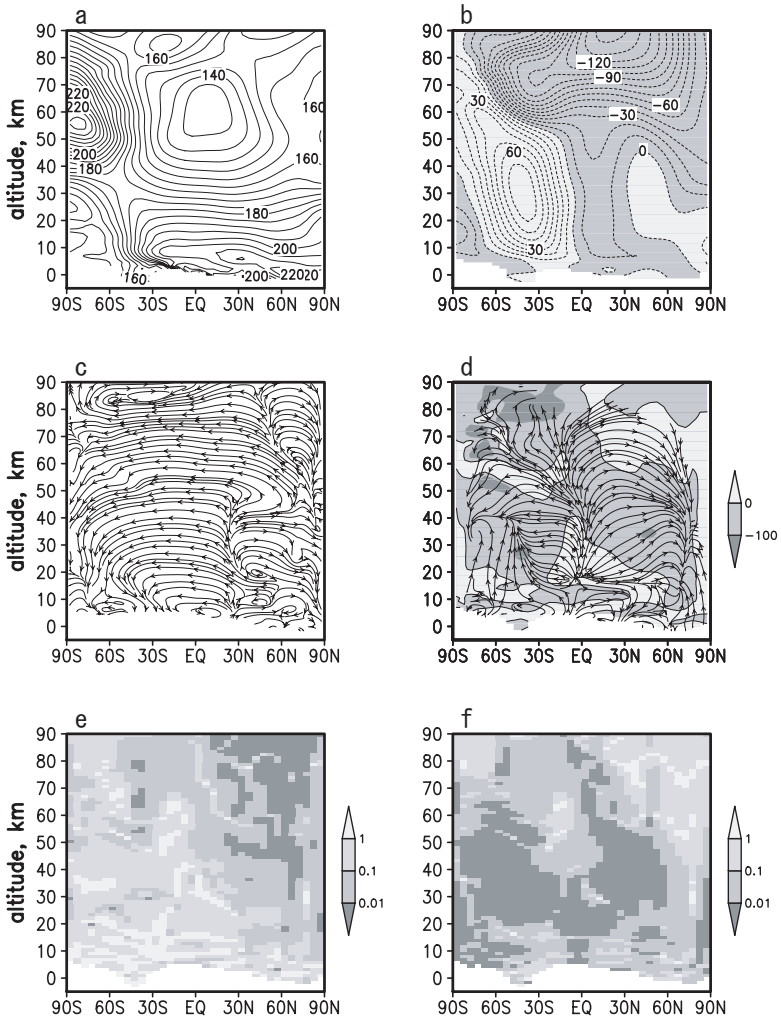


Figure 3.11: Simulation results with the full physics (Run-4) for perpetual $L_s = 90^\circ$ after 40 sols running. (a): the zonal mean temperature with the contour interval 5 K. (b): dotted in shade is for the westward (negative) zonal mean winds, in light is for the eastward (positive) zonal mean winds with the contour interval 10 m s^{-1} . (c): Stream lines of the residual mean zonal circulation. (a): Arrow lines denote the EP flux, and shade is for the negative EP flux divergence. (e): the ratio of the EP flux divergence (Run-3 divided by Run-4). (f): the ratio of the EP flux divergence (Run-2 divided by Run-4).

3.4 Simulation with all Types of Waves Included

Figure 3.11 shows the results for the Run-4. It is seen that, in the summer hemisphere over 30°N and at 30 km height, the clockwise circulation is generated because the negative EP flux divergence enforces the northward flow. The eastward Coriolis force (which arises for the northward flow) compensates for the westward acceleration produced by the negative flux divergence. As the result of the momentum balance, the westward wind near the equator appears. The temperature maximum at 70 km over the summer pole is the result of the combined effect of the diabatic heating (increased solar IR radiation absorption), and the adiabatic heating associated with the downward motions (a smaller clockwise cell). The temperature maximum over the winter pole centered around 60 km is entirely due to the adiabatic heating associated with the downward air flow [Wilson, 1997]. The westward zonal winds cover almost the entire upper atmosphere.

Figure 3.11e,f show, in which area tides or stationary planetary waves (SPW) affect in EP flux divergence; Run-3 divided by Run-4 (panel e) and Run-2 divided by Run-4 (panel f). As a result of Figure 3.11e, SPW generated from only topography propagate to the winter middle hemisphere. While thermally forced SPW induced by the diurnal solar insolation propagate to the upper atmosphere on the equator and the summer hemisphere in Figure 3.11f.

3.5 Baroclinic Waves

An uneven topography triggers not only stationary and gravity waves, but also free Rossby waves, or baroclinic waves. Besides stationary waves forced by the flow over the topography, free modes of planetary waves exist in the atmosphere. These waves are called baroclinic planetary waves. Unlike the stationary harmonics, they can travel in the eastward or westward directions, and therefore sometimes are called the traveling planetary waves. Naturally, their moving peaks and troughs create a non-zero frequency for the observer on the surface. The periods of baroclinic waves are always longer than the period of the planet rotation. Similar to stationary planetary waves, baroclinic waves are excited predominantly in the lower atmosphere, but their energy (wave action) can be transported away and up. Thus, both types of waves propagate in the meridional plane in a similar fashion. Baroclinic waves are generated by the flow instability (“baroclinic instability”), triggered by the topography, or by thermal inhomogeneities [Lindzen *et al.*, 1980]. Baroclinic waves were detected on Mars during the in-situ measurements by Viking Lander 1 (VL1; landed at 50.62°W and 24.92°N in 1982) in mid-latitudes near the surface during the dusty season from $L_s = 200^\circ$ to 300° [Sutton *et al.*, 1978].

According to the VL1, baroclinic waves are strong in the dusty season, but weak during the $L_s = 90^\circ$ season [Hourdin *et al.*, 1995]. Figure 3.12 shows the daily averaged surface pressure oscillations measured by VL1. Figure 3.13 presents the frequency spectrum for these oscillations obtained with the Fast Fourier transform (FFT) around $L_s = 90^\circ, 180^\circ, 270^\circ$ and 360° . Long period waves with the frequencies $\sigma \approx 0.25$ and 0.4 were observed around $L_s = 270^\circ$ and 360° in Figure 3.13. However, they were weak during $L_s = 90^\circ$ and 180° at the VL1 landing site. This means that the lower part of the atmosphere in summers is baroclinically more stable than during winters because of smaller

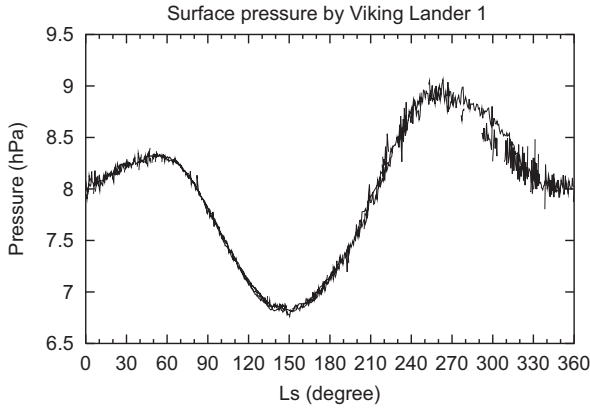


Figure 3.12: Surface pressure detected by Viking Lander 1 (VL1) landing at 50.62°W – 24.92°N .

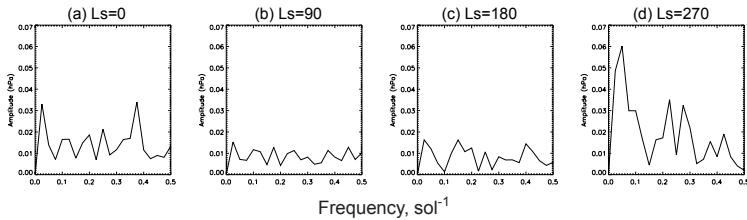


Figure 3.13: The frequencies (sol^{-1}) of the surface pressure from VL1 using the Fourier transform for 20 sols in four seasons, (a) $L_s = 0^{\circ}$, (b) 90° , (c) 180° , (d) 270° . According to (b) and (c), the surface pressure oscillations are too small to be detected because of the weak baroclinic waves depended on latitude.

meridional temperature gradients between the poles and mid-latitudes. As the result, less baroclinic waves are excited during this time in the Northern hemisphere. Generally, baroclinic waves are strong on Mars in the troposphere below 30 km near the prograde jet at mid- to high latitudes in the winter hemisphere. At least two reasons can explain the increase of the baroclinic instability, and as a result, stronger baroclinic wave activity during this time of the Martian year: stronger absorption of the solar radiation by the surface at perihelion, and the enhanced absorption during dust storms normally occurring during this season.

The sensitivity tests presented in Figure 3.14 were designed to explore the effect of the surface. The model was ran for clear sky conditions (no dust heating is included) for the perpetual seasons $L_s = 90^{\circ}$ and $L_s = 270^{\circ}$. The upper row in Figure 3.14 presents

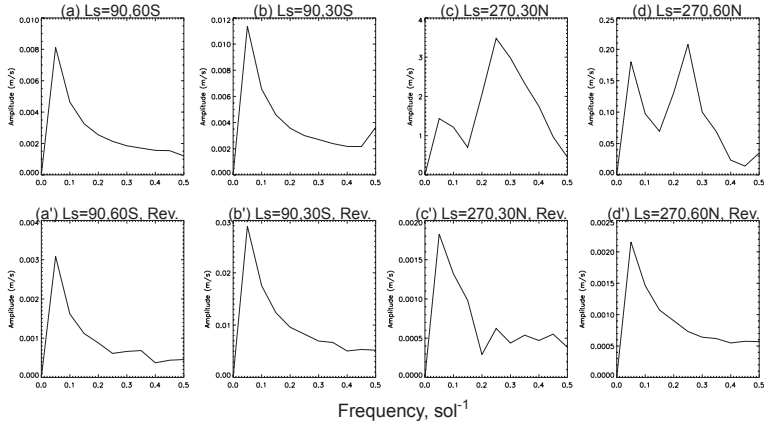


Figure 3.14: Simulation results for amplitude (m s^{-1}) versus frequency (sol^{-1}) of the v -wind near the surface (10 km) in southern winter (a, b, a', b') and northern winter (c, d, c', d') where baroclinic waves becomes strong. Two types of the topography are considered in these experiments: Top panels (a, b, c, d) are for normal topography; bottom (a', b', c', d') are for the north-south reversed topography. Panels (a, b, c', d') show no waves in the winter hemisphere, while panels (a', b', c, d) show some waves.

the frequency spectra for the time series of the v -wind near the point corresponding to the winter hemisphere for the two seasons. It is seen that no long period waves were generated in the winter hemisphere for $L_s = 90^\circ$, whereas a clear and strong planetary wave signal is seen ($\sigma \approx 0.25$) in the winter hemisphere for $L_s = 270^\circ$. The lower row of panels in Figure 3.14 presents the same spectra but calculated from the runs with the topography reversed with respect to the equator. Again, no baroclinic waves are generated during the $L_s = 90^\circ$ winter. For the $L_s = 270^\circ$ winter, the result is strikingly different: very weak wave generation occurs with the reversed topography.

The Martian topography has a definite latitudinal slope with higher lands in the Southern hemisphere, and lower ones in the Northern. *Richardson et al.* [2002] and *Takahashi et al.* [2003] discussed the influence of this inter-hemispheric slope on the meridional circulation. They showed that the differences in the surface heating associated with variations of the optical depth due to the topography are negligibly small. They also demonstrated that the main effect of the tilted lower boundary is the asymmetry of the meridional circulation. Here we extend their analysis by exploring the effect of the asymmetry on the baroclinic instability of the lower atmosphere, and, therefore, on planetary wave generation. For that, it is convenient to use an estimate for the baroclinic growth rate, Kc_i , given by [*Holton, 1992; Takayabu and Takehiro, 2003*]

$$Kc_i = \Lambda f / 2ND, \quad (3.4)$$

where the vertical wind shear, $\Lambda = d\bar{u}/dz$ is proportional to $-d\bar{T}/dy$, f is the Coriolis

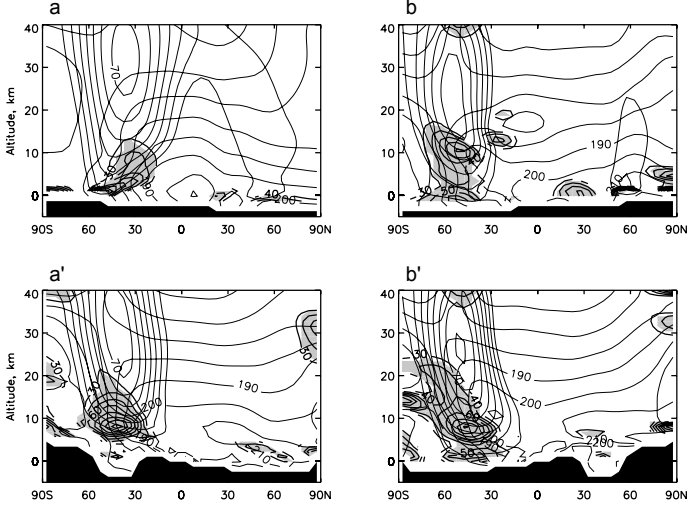


Figure 3.15: Zonally averaged temperature and eastward wind. The shaded areas indicate the growth rate of the baroclinic instability K_{c_i} given by Equation (3.4) for $L_s = 90^\circ$, starting from 30 in intervals of 10. The top panels show the results for a topography consisting of 3 steps with zonally constant heights. The panels (a', b') are for the realistic topography. Right panels (b, b') are for the north-south reversed topography.

factor, D is the atmospheric thickness taken here as 25 km, and N is the Brunt-Vaisala frequency (related to the vertical gradient of the mean temperature):

$$N^2 = \frac{g}{T} \left(\frac{dT}{dz} + \frac{g}{c_p} \right). \quad (3.5)$$

Figure 3.15 presents the distributions of the growth rate K_{c_i} computed from the results of the four sensitivity tests conducted for the perpetual season $L_s = 90^\circ$. In Figure 3.15a,b the MOLA topography was replaced by 3 plateaus with different heights in north-south direction but constant height in east-west direction. The systematic latitude gradients are shown. It is seen that most of the baroclinic wave generation occurs in mid-latitudes of the winter (Southern) hemisphere where the meridional temperature gradient is the steepest, and the wind shear is the strongest. It is seen from Figure 3.15b that, for the idealized topography, wave generation is stronger when the surface height grows towards the Northern hemisphere. The lower panels in Figure 3.15a',b' present the calculated K_{c_i} for the realistic (panel a') and the reversed (panel b') topography. For the realistic topography, the baroclinic wave generation in b' is more remarkable than a', because wind shear is strong if the highland-hemisphere is heated like b'. This is in an agreement with the conclusion from Figure 3.14. On the other hand, this is same as the idealistic case shown in the upper two panels. It is obvious that both latitude and longitude variations of

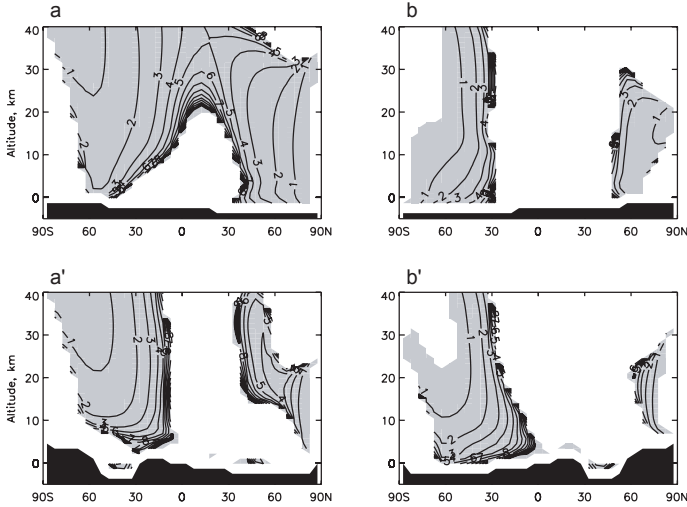


Figure 3.16: Same as in Figure 3.15, but for Rossby wave numbers s given by Equation (3.7).

the surface topography contribute to the shape of the meridional circulation, and, as the result, to the intensity of waves generated near the surface.

3.6 The Influence of the Topography on Wave Propagation

In the end of the above Section 3.5, we considered the effects of the topography on planetary wave generation. In this section, we explore how the topography affects the propagation of the waves once they were excited. For simplicity, we limit our consideration by stationary planetary waves only ($\sigma = 0$), but a similar analysis can readily be extended to traveling (baroclinic) harmonics. For these waves, the propagation condition is given by

$$\bar{u} > 0 \quad (3.6)$$

$$s < a \cos \phi \left(\frac{\beta}{\bar{u}} - \frac{f^2}{4H^2N^2} \right), \quad (3.7)$$

where s is the longitudinal wavenumber of the harmonic, β is the latitudinal gradient of the Coriolis parameter f , H is the scale height, and N is the Brunt-Vaisala frequency in Equation (3.5). Only harmonics with s satisfying (3.7) can propagate vertically.

Figure 3.16 presents the largest longitude wavenumber s for propagating planetary waves calculated for the same conditions as in Figure 3.15. We see from Figure 3.16 that shorter waves (with larger s) are able to propagate near the surface and close to the

equator. Higher and closer to the poles, the propagation condition selects only longest harmonics. For the idealized zonally symmetric topography (panels a,b), more waves can propagate vertically in the case of a South-North surface slope than for the realistic topography (panels a',b'). For the realistic topography, not only the excitation is stronger, but the condition for planetary wave propagation is better for the case in Figure 3.16a,b. Note, that the stationary planetary waves can propagate only in the areas where $\bar{u} > 0$. Traveling waves with $\sigma \neq 0$ can propagate also when $\bar{u} < 0$.

We have shown that the distribution of the topography affects the generation and propagation of planetary waves. In the next section, we consider how the topography affects the zonal mean circulation of the Martian atmosphere.

3.7 The Influence of the Topography on the Mean Circulation

Distributions of isotherms in the Martian atmosphere depend on both the solar heating and the topography and material features on the surface. Our simulations confirm the observations of seasonal asymmetry in the circulation between the two solstices: $L_s = 90^\circ$ and 270° in Sections 3.5–3.6. Under the no dust conditions, the mass stream function (and the related meridional velocities \bar{v} and \bar{w} [Santee and Crisp, 1995]) are 3 times larger during the $L_s = 270^\circ$ solstice. Partially, this is explained by 1.5 times stronger solar radiation flux: 730 W m^{-1} on perihelion ($L_s = 270^\circ$) versus 500 W m^{-1} on aphelion ($L_s = 90^\circ$) due to the eccentricity of the orbit. In explaining the difference in the circulation strength, the remaining factor two can be attributed to the asymmetry in the topography [Smith and Zuber, 1996; Takahashi et al., 2003].

In previous Sections 3.1–3.4, we demonstrated that planetary waves and solar tides in the middle and upper atmosphere have large magnitudes. They are generated mainly near the surface, propagate upward, and deposit the momentum through the convergence of EP fluxes. These waves and tides are important sources of the momentum which maintains the meridional Hadley circulation at these heights. We now turn our attention to the question of how the Martian topography affects the circulation in the lower atmosphere.

Usually, in the inter-tropical convergence zone (ITCZ) on Earth, a low near-surface pressure creates the ascending current, which constitutes an upward branch of the meridional circulation. Similarly, in our $L_s = 90^\circ$ simulation, a low pressure zone resembling the ITCZ gives rise to the Hadley circulation. However, the downward flow in the descending convergence zone (DCZ) in the winter hemisphere is more intense than the upward flow in the ascending convergence zone (ACZ) in the summer hemisphere.

Figure 3.17 presents a series of experiments to study the sensitivity of the meridional circulation to the position of surface inhomogeneities. For simplicity and in order to focus on the effects of the topography only, we turned off the tides by replacing the diurnally varying heating with its daily averaged value. This is done in the same manner as in the experiments Run-2 described in Section 3.2. To specify a disturbance on the surface, we used a zonally symmetric “hill” with the size of one grid step in height and latitude. This corresponds to $\Delta z = 1.14 \text{ km}$ and $\Delta y = 296 \text{ km}$. Figure 3.17 consists of 4 panels (a–d), each panel being composed of two subpanels. Upper subpanels show EP fluxes with arrows, and their negative divergences with shaded areas. The lower subpanels present

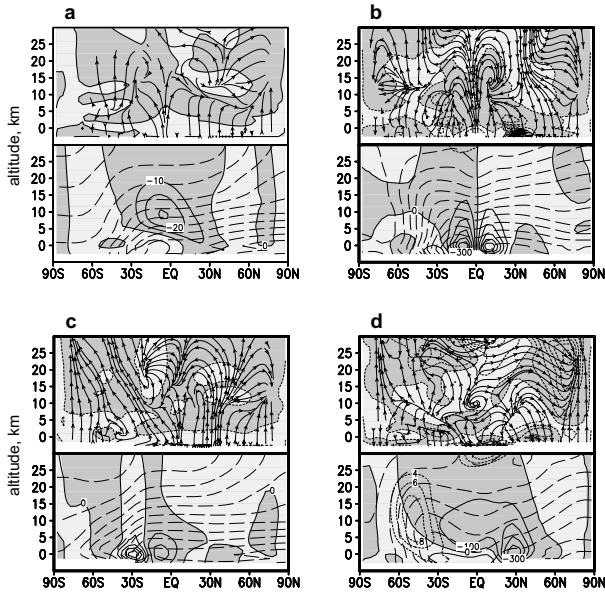


Figure 3.17: Results of the experiments showing the dependence on the topography for $L_s = 90^\circ$ with diurnal solar insolation included. (a): Flat topography everywhere (same as Run-1). (b): Idealized zonal “hill” is placed on equator, 30°S (c), and 30°N (d). Each panel is composed of two subpanels. The upper subpanels show EP fluxes with arrows, and their negative divergences with shaded areas. The lower subpanels present the mean zonal temperatures (dashed lines), and meridional mass stream functions with intervals $100 \times 10^8 \text{ kg s}^{-1}$ (solid lines).

the mean zonal temperatures (dashed lines), and meridional mass stream functions (solid lines). Figure 3.17a displays the results for the flat surface. It is seen that the eddies are generated near the surface mostly as a response to convective instability. They represent normal resonance modes of planetary waves. The magnitudes of these waves are weak, as well as their EP fluxes and the EP flux divergences. The resulted circulation (lower subpanel) is also weak. It represents a direct response to the latitude gradient of the heating. The solid lines in this panel (a) show that the circulation cell is located mainly in low latitudes. This is the so-called thermally induced direct Hadley circulation.

Figure 3.17c presents the results of the experiment in which the “hill” was located near 30°S in the winter hemisphere. This disturbance on the surface generates eddies. The latter propagate upward, dissipate above, and deliver a torque for the meridional circulation. Two cells are seen in the lower subpanel: the clockwise and anti-clockwise ones. The clockwise circulation is directed against the thermally induced Hadley cell, i.e. it tends to weaken the cross-equatorial transport. In Figure 3.17b, we put the surface disturbance on

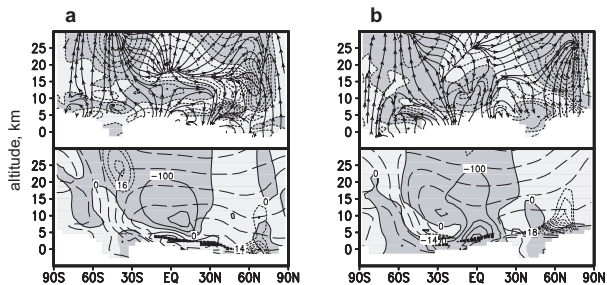


Figure 3.18: Same as in Figure 3.17, but for realistic topography (a), and for the north-south reversed one (b).

the equator. Again, an extensive generation of eddies occurs near the “mountain”. Almost a symmetric two-cell circulation, similar to the equinox circulation in the terrestrial troposphere, is formed in the tropics. Finally, the results for the run with the “hill” at 30°N are shown in Figure 3.17d. The superposition of the two-cell circulation induced by the disturbance on the surface with the thermally direct Hadley circulation produces a highly asymmetric meridional transport. The mechanically induced counter-clockwise cell tends to extend the poleward flow. As the result, a “horn” in the zonally mean temperature is formed in mid-latitudes of Southern hemisphere. The counter-clockwise cell is almost 10 times stronger compared to the pure thermally induced circulation in Figure 3.17a.

In the previous set of experiments, tides were turned off and topography were idealize to highlight the effects of the disturbance on the surface. Figure 3.18 presents the results of simulations with the diurnal solar cycle included. Instead of a small “bump” on the surface, a realistically topography (Figure 3.3) was imposed in these experiments. In this more realistic case, the EP flux divergence associated with the tides and topography forces a stronger meridional circulation. In Figure 3.18a, this topography was set normally, and north-south reversal in Figure 3.18b. Qualitatively, the results are similar to the ones presented above. The disturbance of both experiments induces a large-cell circulation that superimposes the thermally direct Hadley transport. Comparing on Figure 3.18a,b, the disturbance in the summer hemisphere affects the circulation stronger. The clockwise cell is weak and localized, whereas the anti-clockwise cell tends to enhance and extend the Hadley circulation. The isotherms (dashed lines) are formed relied on the topographic trend in comparing bottom subpanels as well as results by *Takahashi et al.* [2003]

3.8 The Local Circulation Induced by Mountains

In the previous Sections 3.5–3.7, we explored the effects of an idealistic zonally symmetric topography on the zonal mean circulation. In this section, we consider the circulation near the surface and the topography effect for the realistic conditions, i.e. limited in both latitudinal and longitudinal dimensions. Mars has tall mountains in low- and mid-latitudes, for example Alba (40°N , 110°W), Olympus (20°N , 130°W), and Tharsis (10°S ,

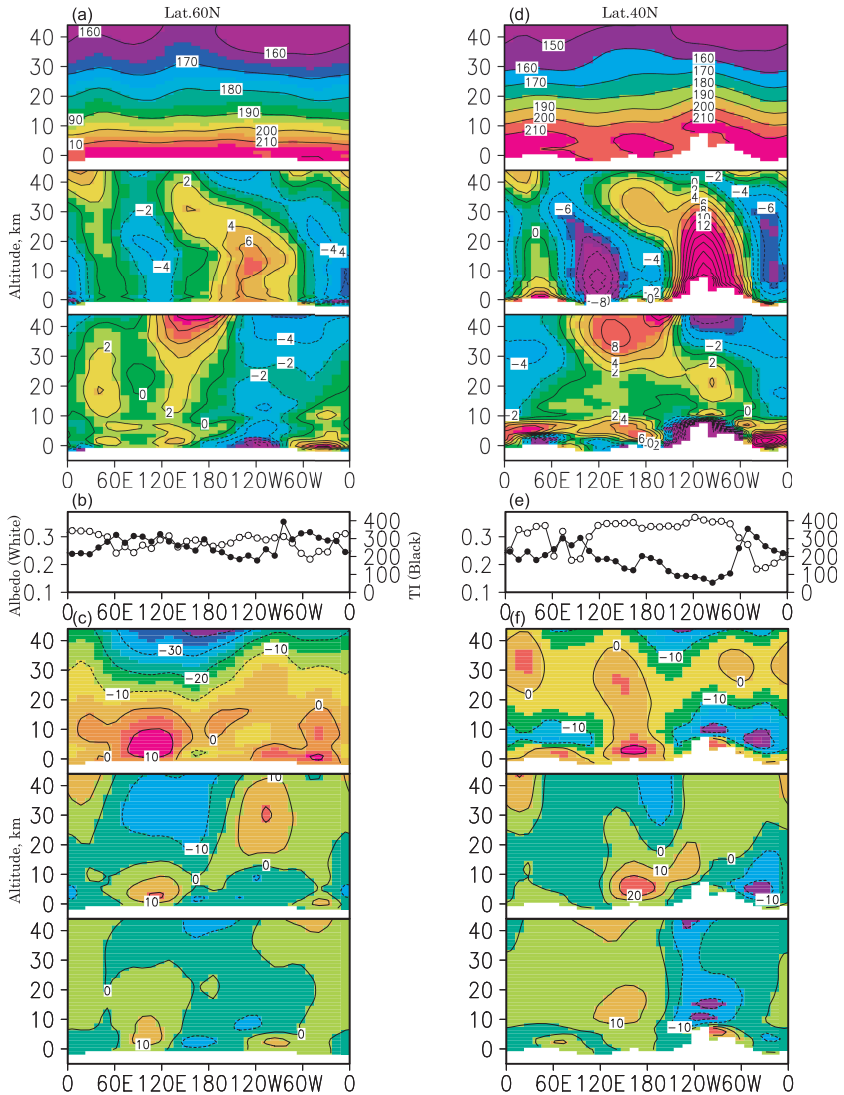


Figure 3.19: Temperature (panels a,d), surface albedo (white dots (b,e)), thermal inertia (black dots (b,e)), and u-wind (c,f) for $L_s = 90^\circ$ at 60°N (a,b,c) and 40°N (d,e,f). Each panel (a,c,d,f) is composed of three subpanels. Top are for the average between day and night: $(2am + 2pm)/2$. Middle is the deviation: $2pm - 2pm^x$. Bottom is the deviation: $2am - 2am^x$.

3 Simulation Results

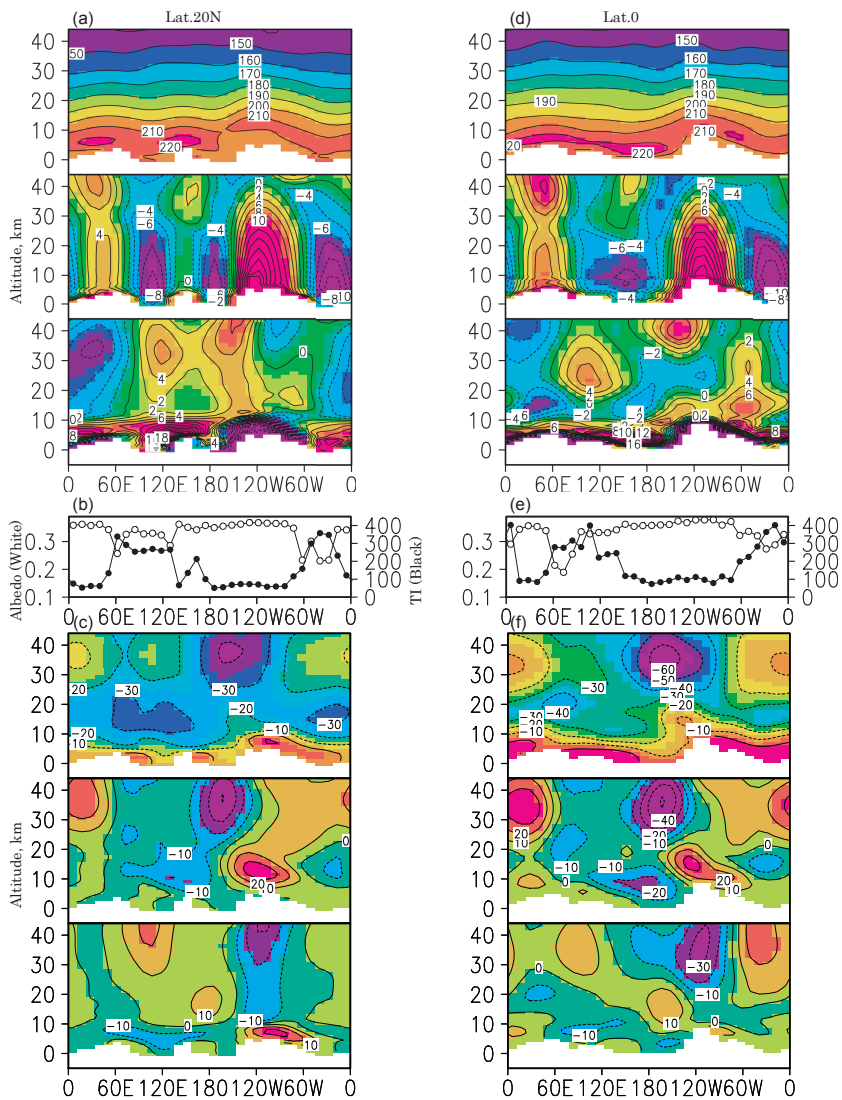


Figure 3.20: Same as in Figure 3.19, but for 20°N and 0°.

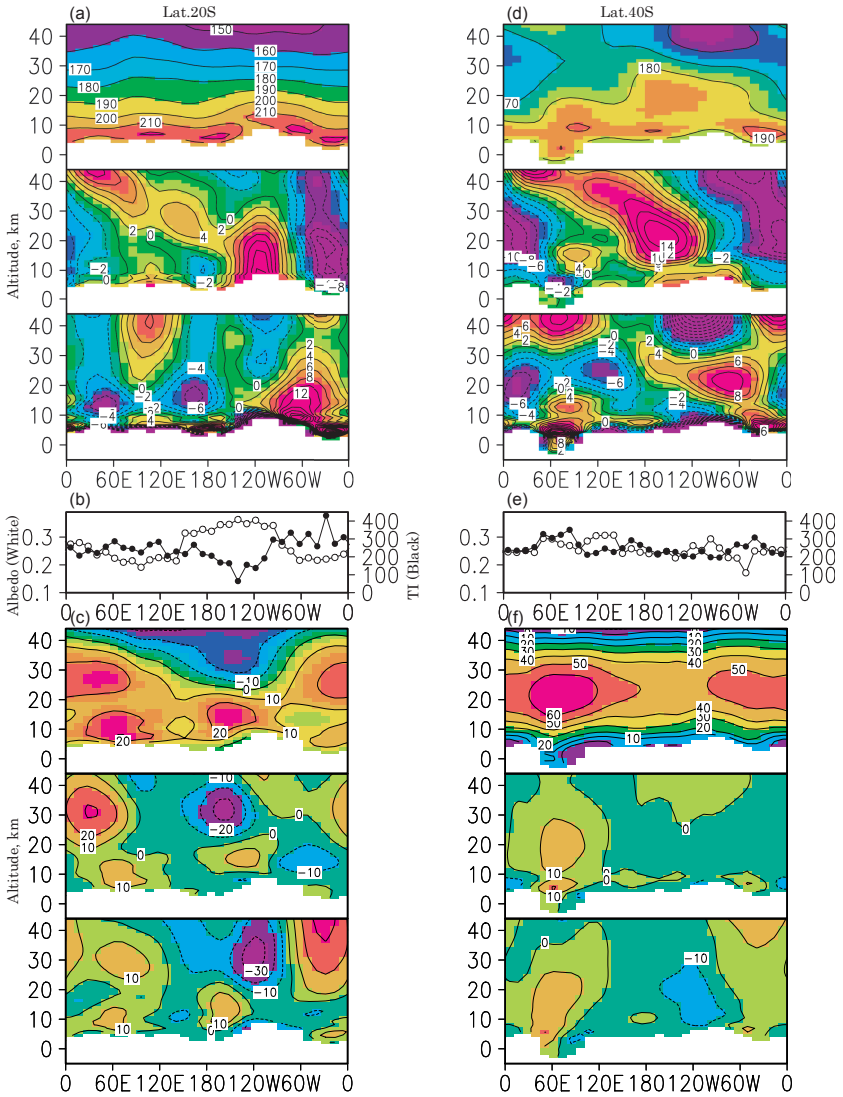


Figure 3.21: Same as in Figure 3.19, but for 20°S and 40°S.

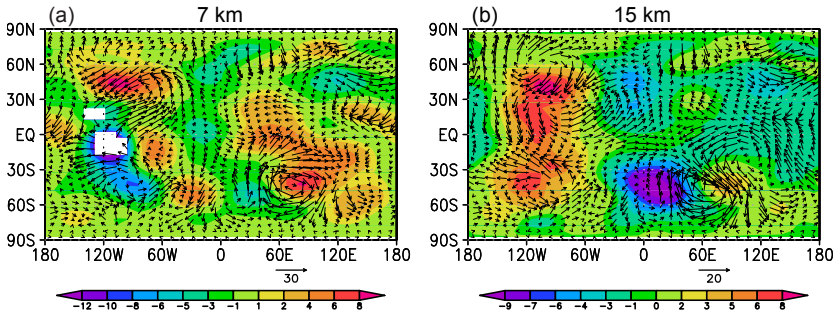


Figure 3.22: Time averaged temperature disturbances ($\overline{T - T^x}$) and the wind field ($\overline{V_{u,v} - \overline{V_{u,v}^x}}$) at 7 km (a) and 15 km (b).

120°W) in Figure 1.2. At low latitudes, Olympus and Tharsis can significantly block the dominant zonal wind, and the Martian bore waves were confirmed by *Pickersgill* [1984]. In low- and mid-latitudes, daily variations of the surface temperature and wind at and near the surface are very strong during summers [*Joshi et al.*, 1997].

Longitudinal variations of the atmospheric fields simulated in the control run with the “full” physics are presented in Figures 3.19–3.21. The model output was processed in a manner to imitate the measurements taken from Mars Global Surveyor (MGS). MGS is on a polar orbit, and observes the atmosphere and surface at almost the same local time: 2 pm and 2 am. We also selected only the fields corresponding to 2 pm and 2 am to study their longitudinal dependences.

Figures 3.19–3.21a,d (second subpanel) present the difference between the daytime temperature and the daytime averaged temperature ($T_{2pm} - \overline{T_{2pm}^x}$). It is seen that, during the daytime, atmospheric air is hotter over the mountains. The strongly heated mountain surface contrasts with the relatively cold surrounding air. Convective fluxes and/or upwelling transport the heat up, and create areas of warm temperature over the mountains. During nighttime (2 am), the surface cools down faster than the surrounding air [*Blumsack et al.*, 1973]. This leads (third subpanels in Figure 3.19–3.21a,d) to nighttime temperature inversions over tall mountains. These inversions are not that persistent compared to the daytime warming, but they create distinctive circulation patterns around mountains. The first subpanels in Figures 3.19–3.21c,f present the daily mean longitudinal wind, u , and the daytime (second subpanels) and nighttime (third subpanels) deviations ($u_{2am,2pm} - \overline{u_{2am,2pm}^x}$). It is seen that the horizontal wind is also affected by mountains. When the background wind is eastward, positive temperature disturbances propagate upward from the top of the mountain in second subpanels of Figure 3.21a,d.

Longitude-latitude wind distributions near the surface are shown with vectors in Figure 3.22. Similar maps were presented in the simulation studies by [*Leovy and Mintz*, 1969; *Barnes et al.*, 1996; *Fenton et al.*, 2001]. They compare well with the simulations with our model. Figure 3.22a shows the atmospheric temperature disturbance and winds disturbance at 7 km height, and panel (b) is for at 15 km. Persistent vortices are

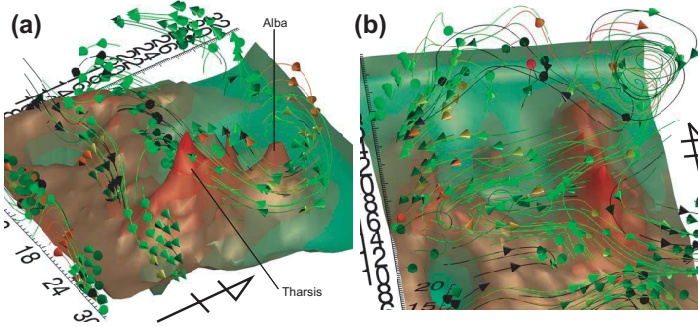


Figure 3.23: Martian winds stream lines in 3D simulation with the topography at 11 km (a), and 22 km (b). Axis numbers show the grid points in our model. Surface color red means high and green means low.

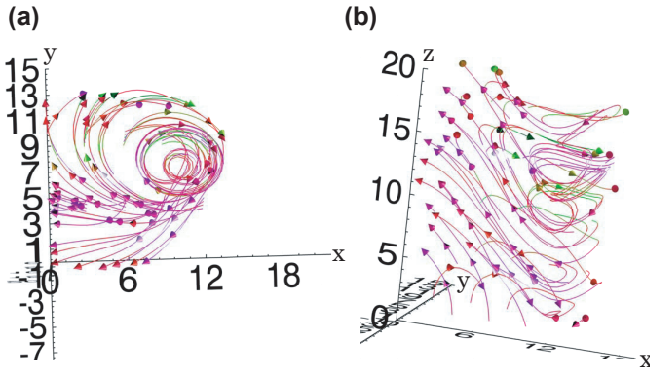


Figure 3.24: Wind field from Figure 3.23 between 180°E and 360°E, and between 0° and 90°N around Alba (40°N, 110°W) and Olympus (20°N, 130°W).

seen around Alba (40°N, 110°W) and the basin Hellas at (70°E, 40°S). The direction of the wind velocities in these vortices at 15 km (panel b) are consistent with anticyclones (high-pressure) and cyclones (low-pressure), respectively. These persistent wind and temperature disturbances are the manifestation of stationary planetary waves in the lower atmosphere. 3-dimensional plots in Figure 3.23 visualize the nonzonal nature of the near surface circulation. It is clearly seen from Figure 3.23a that the clockwise circulation dominates around Alba, and the upwelling over the Olympus and Tharsis is strong. There, Olympus and Tharsis are painted with red color. According to Figure 3.23b which shows the fields below 22 km, the spiral wind trajectories are tilted eastward with height. This

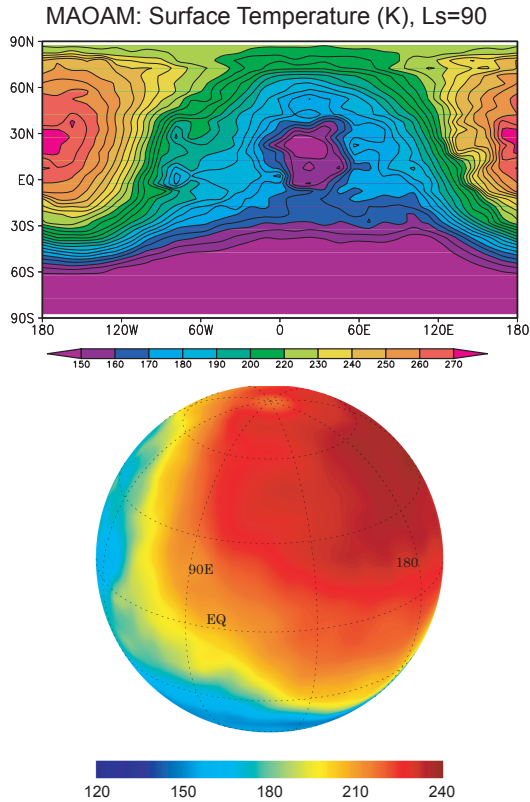


Figure 3.25: Simulated surface temperature for $L_s = 90^\circ$ at noon.

flow gets stronger near the equator and goes up along the slope, as shown in Figure 3.24b. The westward winds on the equator have to climb and detour the mountain. Then the winds turn finally left, and turns out strong eastwards winds in mid-latitudes of the winter hemisphere. Therefore, strong upwelling above Olympus and Tharsis is resulted from the forced clockwise circulation around Alba.

3.9 The Surface Temperature

The global thermal inertia and surface albedo of Mars has been investigated by *Putzig* [2005] in detail, in particularly the relationship between the surface properties and the surface temperature. Indeed, the surface temperature strongly depends on elevations [*Molnar et al.*, 1999]. In this section, we consider interactions between the surface and near

surface atmosphere. The main emphasis here is made on the influence of varying topography, thermal inertia and albedo on the generation of temperature disturbances in the atmosphere. A relevant study of the relationship between the temperature surface and the thermal inertia will be considered in the Section 4.4.

The surface temperature depends on the thermal inertia I and surface albedo A , for details see Section 2.4.3. In areas with a large I , the surface temperature remains warmer even during nights. This is similar to the terrestrial ocean with large thermal capacity, I is proportional to the square root of the thermal capacity. The range of temperature variation during day and night depends on I . The surface albedo A controls the ratio between the reflection and absorption of the solar flux. For small A , the solar absorption on the surface is weak.

Figures 3.19–3.21b,e present the global thermal inertia and surface albedo prescribed from observations [Mellon, 2003]. In the top panel (Figures 3.19–3.21a,b), the atmospheric temperature near the surface around mountains is smaller than in the basin. In general, the diurnally averaged atmospheric temperature tends to decrease with height, such that the temperature near the surface is usually the hottest in the entire vertical column. However, temperature inversions at some places have been detected in the radio science (RS) occultation experiments [Hinson *et al.*, 2003; Hinson *et al.*, 2004]. These measurements have usually higher vertical resolution compared to TES. Meanwhile, TES has also detected temperature inversions around the mountain at 60°E and 120°W. This will be discussed in the next chapter.

In the second subpanels in Figures 3.19–3.21a,b, where daytime temperatures disturbance are shown, the surface temperature is especially large near the top of the mountains, where I is small. This can easily be understood since, when heated, the surface temperature tends to rise faster in areas with the smaller I . During days, an overheated (in areas with the small I) surface can cause a convection, which, in turn, reduces lapse rates. On the other hands, in the third subpanels, where the nighttime temperatures disturbance are shown, the surface temperature sharply decreases in the areas of small I . For the conditions of small I /large A (i.e. for small ratios I/A), even the daily averaged surface and near surface atmospheric temperatures cool down faster than the air above. The net effect of this can be vertical temperature inversions over the areas with small I/A at the surface.

These peculiarities of the surface characteristics can result in a generation of stationary planetary waves, and the subsequent wave energy propagation in the atmosphere. The westward and upward propagation of the hot temperature disturbances generated over the surface on the mountain slope in the Southern hemisphere is seen second subpanels in Figure 3.21a,d, but in the Southern hemisphere. These differences of the energy propagation depending on the latitude are due to refractive properties of the mean circulation. The latters are mainly the functions of the mean zonal wind, as explained in Section 4.3.

Comparison of the second and third subpanels reveals the differences between day- and nighttime temperature disturbances in Figure 3.20–3.21a,d. During the day (second subpanel), the disturbances propagate mostly in the vertical direction, while during the nights (third subpanel), the wave train paths are tilted with height. The strong convection occurring during the daytime helps to extend the temperature disturbances vertically, but during nights, when there is no or very weak convection, vertical propagation is inhibited. The influence of the convection appears to be stronger than that of the topography and local winds, therefore the vertical propagation dominates. Without the convection, only a

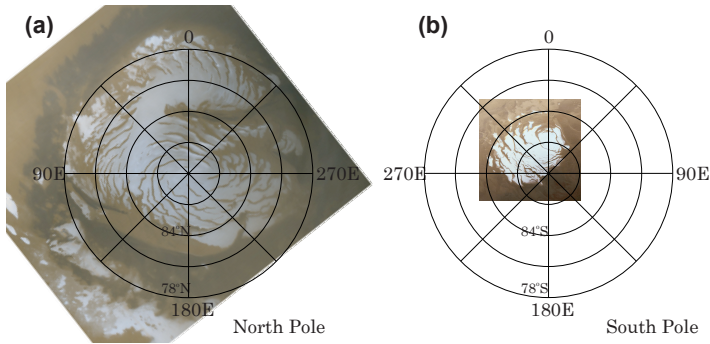


Figure 3.26: Both polar views are taken by satellite observations during the Martian summer season. (a): The Northern polar cap is largely composed of frozen water after carbon dioxide ice sublimates. This view of the cap was obtained by Mars Global Surveyor during the northern summer. The cap is roughly 1095 km across. (b): The Southern polar cap is composed of carbon dioxide ice. This view was obtained by the Viking Orbiter.

dynamical generation of disturbances (the flow over the topography) takes place.

3.10 The Influence of the Polar Caps

Polar caps cover both polar regions of Mars. The Southern polar cap is composed of almost pure CO_2 , and the Northern polar cap consists of 85 percent CO_2 and 15 percent H_2O [Langevin *et al.*, 2005; Hansen *et al.*, 2005]. The polar cap temperature depends on the ratio of CO_2 and H_2O . The average Northern polar cap temperature is 146 K, and the Southern one is 142 K [Paige and Ingersoll, 1985].

During the $L_s = 90^\circ$ season, the diameter of the Northern polar cap in summer is 1100 km, but CO_2 in the cap almost vanishes, and H_2O remains, while the Southern polar cap grows in winters. On the other hand, during the $L_s = 270^\circ$ season, the diameter of the Northern polar cap grows, while the Southern polar cap shrinks to an average 420 km. According to Figure 3.26, the area covered by both caps varies depending of the season. Around $L_s = 90^\circ$ (northern summer and southern winter), the Northern polar cap shrinks up to 80°S latitude, and the Southern cap expands up to 40°N . At the $L_s = 270^\circ$ season, the Northern cap extends up to 40°N , and the Southern one shrinks to 85°S . Hence, the interactions of the atmosphere with the surface must be considered, especially since the surface temperature contrasts due to the caps represent the source of forced stationary planetary waves. These waves generated near the polar caps were detected by MGS-*TES* [Colaprete *et al.*, 2005; Fukuhara and Imamura, 2005].

The polar caps formation is different for each hemisphere because of the large eccentricity of the Martian orbit. The distance of the planet from the Sun at $L_s = 90^\circ$ is farther than at $L_s = 270^\circ$. Therefore, Southern polar cap variations are greater than at

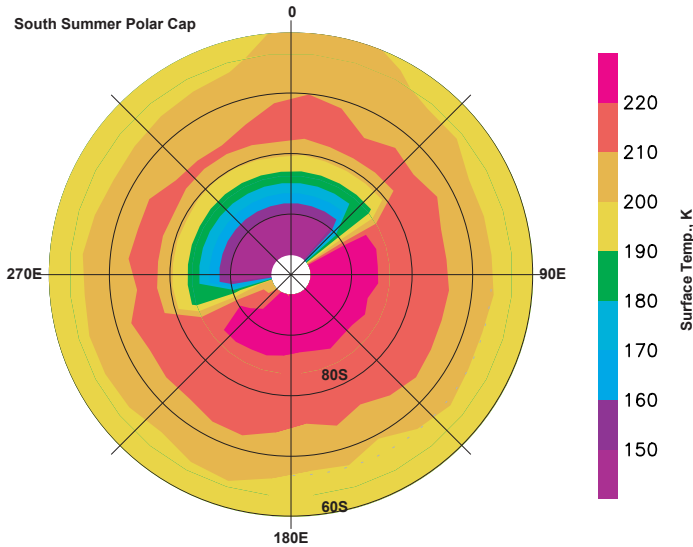


Figure 3.27: Simulated surface temperature on the Southern polar cap during southern summer ($L_s = 270^\circ$).

the Northern one. This means that a greater amount of ice evaporates during the southern summer ($L_s = 270^\circ$) and condenses during the Southern winter ($L_s = 90^\circ$). On the other hand, the area covered by the Northern cap almost does not change with seasons [Pollack *et al.*, 1990]. The dissolving of the Southern cap occurs with the longitudinal asymmetry [Paige *et al.*, 1994, Paige and Keegan, 1994], and this asymmetry (Figure 3.26b) modifies the temperature and circulation, especially during southern summers [Fukuhara and Imamura, 2005].

To estimate the influence of the polar cap contrasts on the atmospheric temperature and winds, we designed four numerical experiments for $L_s = 270^\circ$: (A) only the topography and the solar cycle were taken into account, (B) the imposed surface temperature prescribing the Southern polar cap was added to (A), (C) the surface albedo and thermal inertia were added to (A), (D) combines all the features of (A), (B), and (C). The simulated atmospheric temperatures in Figure 3.29 were obtained at 2 pm and 2 am local times in line with the TES measurements [Banfield *et al.*, 2003, Fukuhara and Imamura, 2005]. The figure consists of four panels for each experiment from (A) to (D). The top subpanels in the figure present stationary waves determined as $T_m = (T_{2am} + T_{2pm})/2$. The middle and bottom subpanels show the disturbances of the temperature during for daytime, $T_{2pm} - \bar{T}_{2pm}$, and nighttime, $T_{2am} - \bar{T}_{2am}$, respectively. The u- and w-components of the wind are plotted in the same manner in Figures 3.30 and 3.31 respectively.

The surface temperature on the Southern cap (including the zonal asymmetry) was set to the constant value of 146 K [Forget *et al.*, 1996]. In other words, a time independent

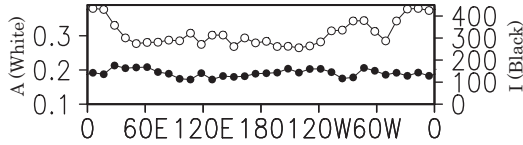


Figure 3.28: The surface albedo (white) and thermal inertia (black) at 80°S.

geographical distribution of the cap was presumed. The initial constant surface temperature distribution corresponds to the cap in Figure 3.26b and simulation result after running 3.27, i.e. the ice is assumed to cover the territory from 100°W to 40°E, and from 90°S to 80°S. The temperature in the grids surrounded the cap are set to 187 K, i.e. equal to the evaporation temperature of the carbon dioxide.

Figure 3.29A (first subpanel) shows the longitudinal disturbance $s = 2$ (the temperature maximum near 30°E and 150°W) which appears exclusively due to the mountain terrace. According to the first subpanel in Figure 3.31A, this column temperature disturbance is the result of a strong downwelling flow caused by the step in the topography. All other longitudinal disturbances (except for the temperature maximum at 150°W) are associated with the tides. For example, the hot temperature band from 150°W at 20 km to 30°E at 40 km at 2 pm (second subpanel) shifts from 30°E at 20 km to 150°W at 40 km at 2 am (third subpanel). Similarly, the cold spot above 60°W at 30 km at 2 pm moves to 120°E at 30 km at 2 am. Figure 3.30A also confirms that the u-wind disturbances are associated with the stationary wave and tides. For tides, some oscillation are detected, for example, the eastward wind area at 60°E at 10 km, and the westward wind at 40 km at 2 pm is replaced by a reversed pattern at 2 am.

In Figure 3.29B (first subpanel), the stationary wave remarkably appears near the surface when the longitudinal asymmetry of the Southern polar cap is introduced. Its magnitude is twice as large compared to the disturbance at 30 km. Figure 3.30B shows that the u-wind is smoother than for Figure 3.30A. This is because the wind shear over 120°W in Figure 3.30B is smaller, and a new area of the upwelling is generated above the terrace on the polar cap 150°E in Figure 3.31B.

Results of (C) are similar to (A), but a comparison of the second subpanels during the daytime shows that the magnitude of the temperature disturbance in (C) is somewhat larger than in (A). It is caused by a stronger absorption of the solar radiation due to the lower albedo in the area around the terrace (60°E–120°W) in Figure 3.28.

Consideration of the results for the case (D) (which effectively is the sum of (A), (B) and (C)) shows the following. First, the downwelling near the terrace step at 150°W produces the vertically extended positive temperature disturbance. Second, the asymmetrical polar cap generates the strong stationary planetary wave near the surface. And third, other waves seen in the simulations are caused by the tides. The main conclusion of the simulation results presented in this section is that the longitudinal asymmetry of the Southern polar cap enforces a strong stationary planetary wave near the surface, which, however, does not propagate high enough.

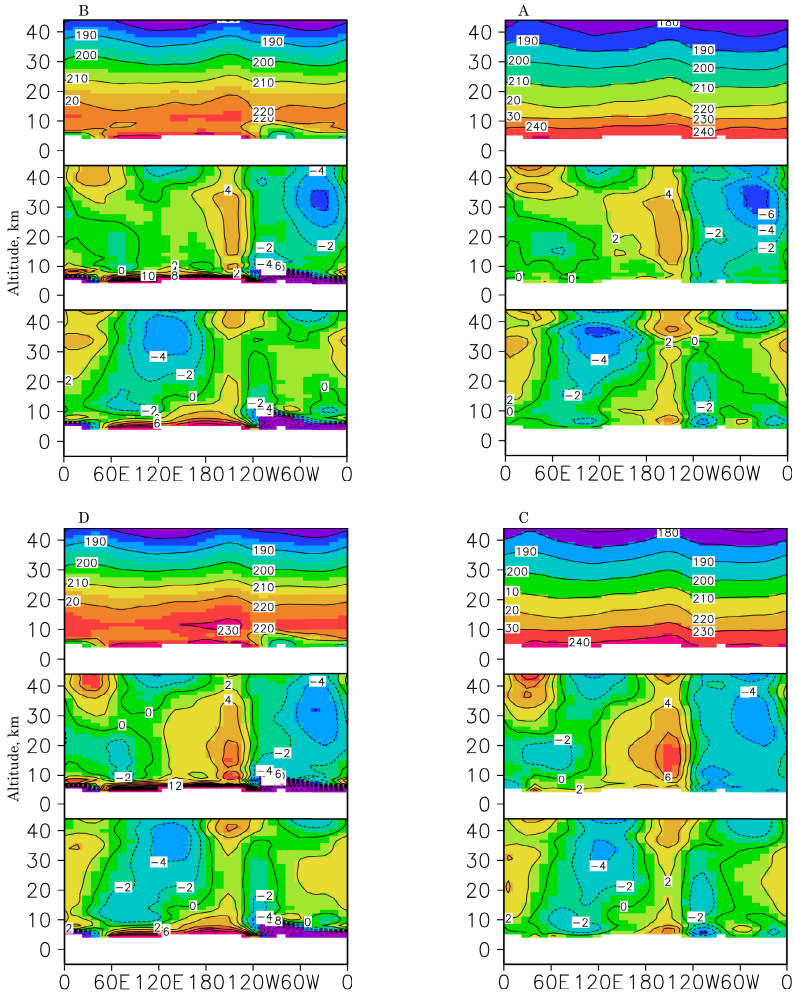


Figure 3.29: Atmospheric temperature during $L_s = 270^\circ$ at 80°S . (A) denotes the result considering only the topography and solar cycle. (B) the polar surface parameterization is added to (A). (C) the surface albedo and thermal inertia are added to (A). (D) is for the “full physics” Run: (D) = (B) + (C). Each panel is composed of three subpanels. Top is for the average between day and night: $(2am + 2pm)/2$. Middle is for the deviations: $2pm - 2\overline{pm}^x$. Bottom is for the deviations: $2am - 2\overline{am}^x$.

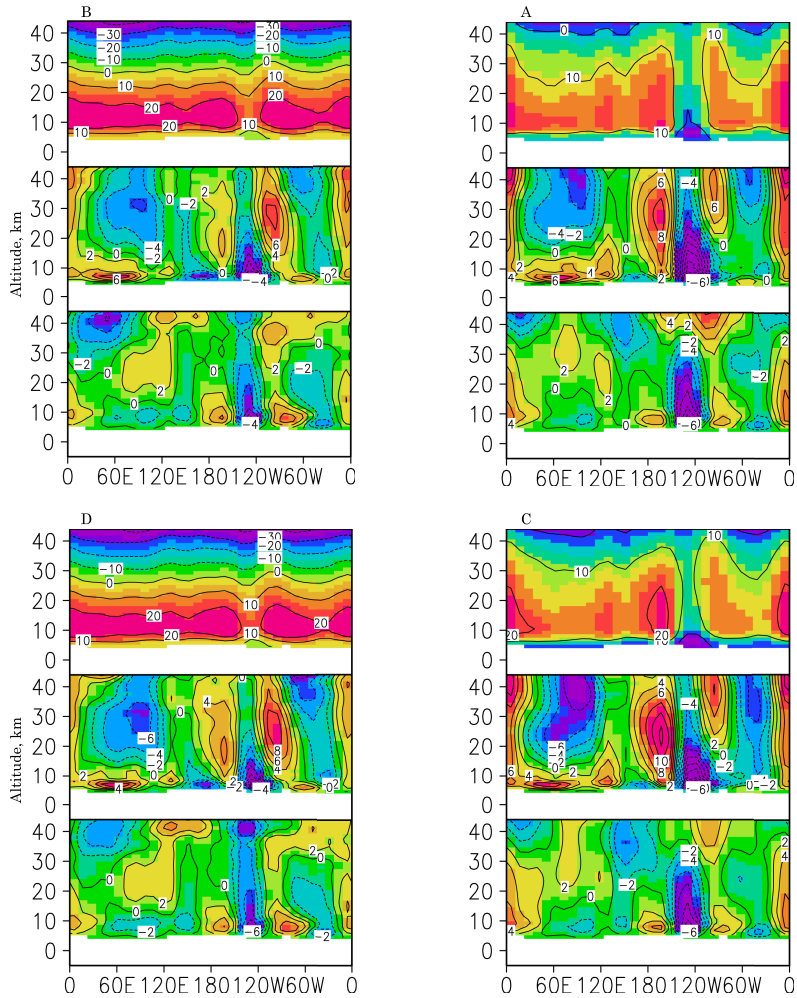


Figure 3.30: Same as in Figure 3.29, but for the u-wind.

4 Comparison of the Simulations with Measurements

4.1 Introduction

In the previous Chapter 3, we presented the results of simulations with the general circulation model of the Martian atmosphere described in Chapter 2. In this chapter, we compare the simulations with available measurements, and discuss the performance of the model.

The most extensive set of air and surface temperature measurements was provided by the Thermal Emission Spectrometer (TES) onboard Mars Global Surveyor (MGS) [Banfield *et al.*, 2000; Conrath *et al.*, 2000]. We processed and analyzed the global data from the nadir observations. MGS-TES observed the atmospheric and surface temperature at fixed local times (2 pm and 2 am) all over the globe. The description of the satellite's orbit, the instrument itself, and the discussion of the temperature retrievals was provided by Christensen *et al.* [1992, 1998] and Zhang *et al.* [2001]. Temperature disturbances associated with stationary planetary waves (SPW) can be extracted from the measurements as $(T_{2pm} + T_{2am})/2$ [Banfield *et al.*, 2003; Hinson *et al.*, 2004]. Day- and nighttime temperature disturbances due to SPW are determined as $T_{2pm} - \overline{T}_{2pm}^x$ and $T_{2am} - \overline{T}_{2am}^x$, respectively. For this chapter, the model output was processed in the very same way to make the direct comparison with MGS-TES possible.

4.2 The Zonal Mean Temperature

First, we compare the simulated zonal mean climate with the observations. Figure 4.1 presents the temperature deduced from the nadir measurements by TES (the right panels), and the model temperatures in the corresponding vertical domain (the left panels).

The Figure 4.1 of $L_s = 90^\circ$ shows an overall agreement in magnitudes and patterns of the temperature fields. The discrepancies near the surface may partly arise due to differences in the zonal averaging procedures in the model and observations. It is important to note that the vertical resolution of TES near the surface decreases, and is about 10 km. In the Southern hemisphere, the model successfully captures CO₂ freezing surface temperatures up to approximately 60°S, the strong meridional gradients in mid-latitudes, and the polar minimum.

Since the meridional gradients of the diabatic heating/cooling rates are weaker at equinoxes, the circulation for $L_s = 180^\circ$ is less robust. Forget *et al.* [1999] pointed out the sensitivity of the simulated equinox circulation patterns to the dynamical core of

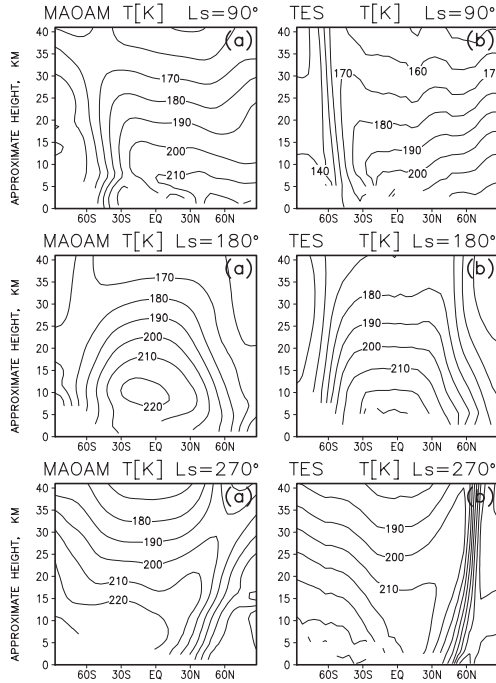


Figure 4.1: Top panels are zonal mean temperature for $L_s = 90^\circ$ (a) simulated with the model, (b) obtained from the TES measurements. The contour interval is 10 K. Middle panels are for $L_s = 180^\circ$ and bottom for $L_s = 270^\circ$.

the model, or, ultimately, to the ability of the model to resolve the eddies. The results of our simulations for $L_s = 180^\circ$ are compared with the TES temperature measurements in Figure 4.1 of $L_s = 180^\circ$. A very good agreement in zonal mean temperatures is seen in almost the entire domain except over the poles. In the low- and mid-latitudes, the difference hardly exceeds the errors associated with the TES [Smith *et al.*, 2001], while on the poles, it is around 10–15 K. Note that the maximum of temperatures in the low latitudes occurs not on the ground but about 10 km higher. Similar features are seen at some temperature profiles retrieved by radio occultation from the MGS [Hinson *et al.*, 1999].

Due to the eccentricity of the Martian orbit, the meridional gradients of the CO_2 radiative heating/cooling are stronger during the southern winter solstice. Dust storms occur at and around $L_s = 270^\circ$, therefore radiative effects of the aerosol are significant, and must be taken into account. The result in Figure 4.1 of $L_s = 270^\circ$ was obtained employing the dust scenario described in [Hartogh *et al.*, 2005]. An overall agreement between the simulated and observed zonal mean temperature is seen in the figure. The major difference is in the location of the area of strong meridional temperature gradients. In the

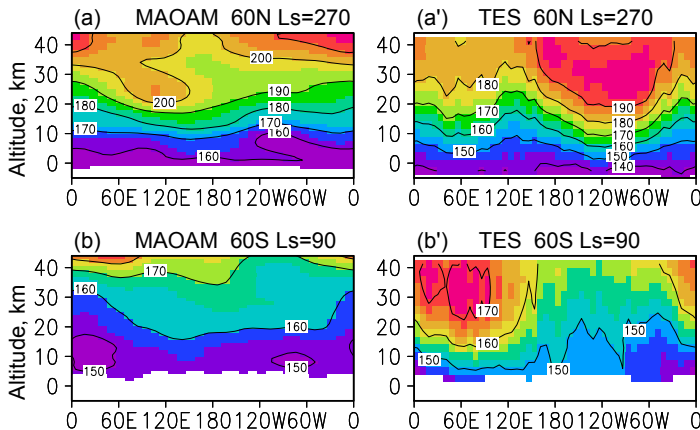


Figure 4.2: Temperature longitudinal variation for the stationary waves: $(T_{2am} + T_{2pm})/2$ for 60°S in $L_s = 270^\circ$ (a, a') and for 60°N in $L_s = 90^\circ$ (b, b'). Model results in (a, b) and TES measurements in (a', b'). The contour interval is 10 K.

simulations, it is somewhat shifted towards the equator compared to the TES data. In our simulations with higher dust opacities, we find that the atmospheric temperatures below 40 km become colder.

4.3 Longitudinal Disturbances in Mid- and High Latitudes

If the circulation was pure zonal, then the distributions of $(T_{2am} + T_{2pm})/2$ would be independent of the longitude. However, *Banfield et al.* [2003] found noticeable longitudinal disturbances in the TES data with $s = 2$ at 60°N around the $L_s = 270^\circ$ season, and with $s = 1$ at 60°S around $L_s = 90^\circ$. These disturbances can be associated with stationary planetary waves. We processed the TES data in a similar fashion as *Banfield et al.* [2003] (but without further expanding into the longitudinal harmonics), and plotted the result in Figure 4.2. Our simulations also produced stationary harmonics with $s = 2$ at $L_s = 270^\circ$ and $s = 1$ at $L_s = 90^\circ$ in Figure 4.2a,b, however with the peaks shifted longitudinally by about 30° eastward for the $L_s = 90^\circ$ simulation. This may be partially explained by differences between the simulated and real (not measured by TES) mean zonal wind. The wave refraction is very sensitive to this wind, and therefore, the phases of the waves can vary in simulations depending on the zonal mean stratification. At other latitudes at $L_s = 90^\circ$ in Figure 4.4 and 4.5, the agreement between the simulated and measured planetary waves is more favorable. The temperature at $L_s = 270^\circ$ was taken from the simulation without the dust. This can explain generally higher simulated temperatures. However, the longitudinal structure is clearly seen in Figure 4.2a despite a different coloring scheme compared

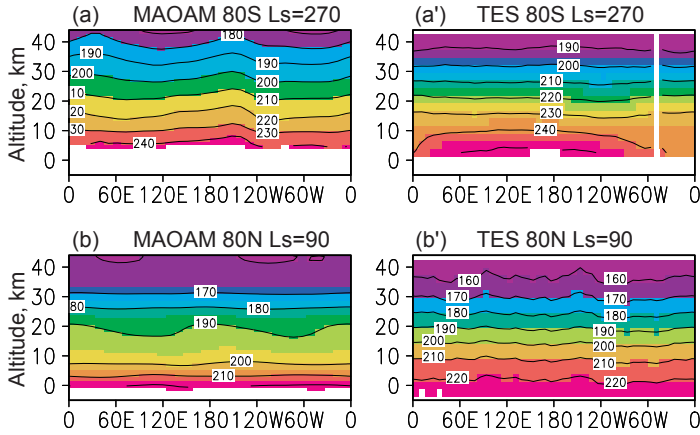


Figure 4.3: Same as in Figure 4.2 but for the summer polar region at 80°N for $L_s = 270^\circ$ (a,a') and at 80°S for $L_s = 90^\circ$ (b,b').

to Figure 4.2a'

Figure 4.3 presents the analysis of the simulations and MGS–TES for high latitude summer hemispheres at $L_s = 90^\circ$ and $L_s = 270^\circ$. Again, $(T_{2am} + T_{2pm})/2$ are plotted in the figure. The agreement is generally good, except for the magnitudes near the surface. For example, the simulated low level atmospheric temperature ranges from 120°W to 60°E , i.e. the area not covered by the polar ice cap, is about 10 K colder (240 K) than the TES data show (250 K). This longitudinal disturbance with $s = 1$ below ≈ 10 km was studied by *Fukuhara and Imamura* [2005]. The other difference is seen between 20 and 40 km for the both summer polar regions. A strong wave $s = 2$ appears in the simulations, and is absent in the TES data.

Figures 4.4 and 4.5 show the longitudinal cross-sections for $(T_{am} + T_{pm})/2$ for the other latitude bands during the dustless season. The model successfully reproduces temperature inversions over the mountainous regions. As was discussed in Chapter 3, these inversions have been detected in Radio Science (RS) experiments [*Hinson et al.*, 2004]. These inversions are clearly seen in the simulations (Figure 4.4b and c) over big mountains. However, it is difficult to find inversions in zonal mean temperature in the TES measurements. Mostly this is due to the fact that the vertical resolution of TES is too low near the surface ($\Delta z \approx 10$) km, i.e. close to the atmospheric scale height [*Hinson et al.*, 2004].

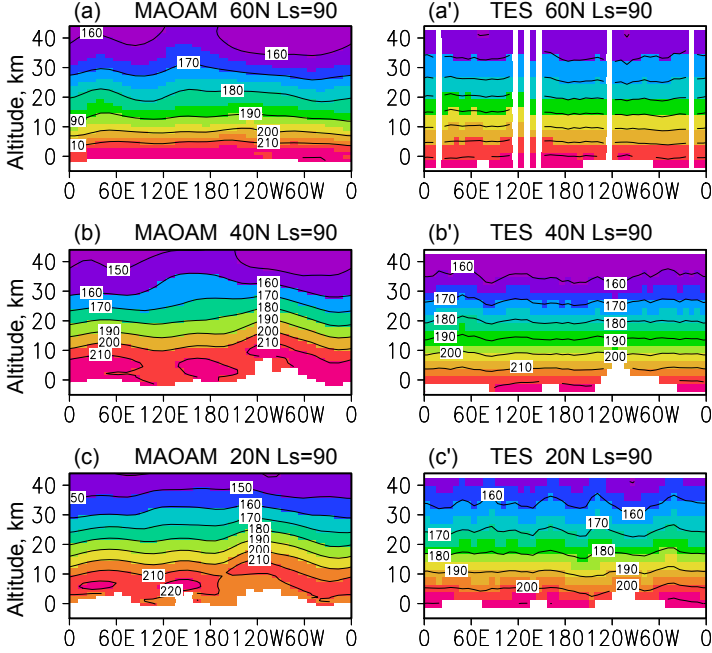


Figure 4.4: Same conditions as in Figure 4.2, but for the latitudes 60°N , 40°N , and 20°N during the $L_s = 90^\circ$ season.

4.4 The Relation of the Surface Temperature with the Thermal Inertia and Albedo

To explain how near surface temperature inversions are related to the surface thermal characteristics, we analyze the surface temperature global distributions at 2 pm and 2 am obtained from the MGS–TES data.

Temperature inversions tend to appear in areas of a strong cooling during nighttimes. We denote a zonally averaged temperature as \bar{T}^x . Then, the surface temperature disturbance T' defined as

$$T' = (T_{2pm} - \bar{T}^x) + (T_{2am} - \bar{T}^x) \quad (4.1)$$

would be equal to zero if the cooling at night (2 am) was balanced by the daytime heating (at 2 pm). Therefore, negative disturbances T' indicate regions of a strong net surface cooling where temperature inversions tend to occur. As was described in Section 3.9, these inversions depend on the ratio of the surface albedo A and thermal inertia I , i.e. on I/A . For example, the surface is colder when I/A is small, and vice versa.

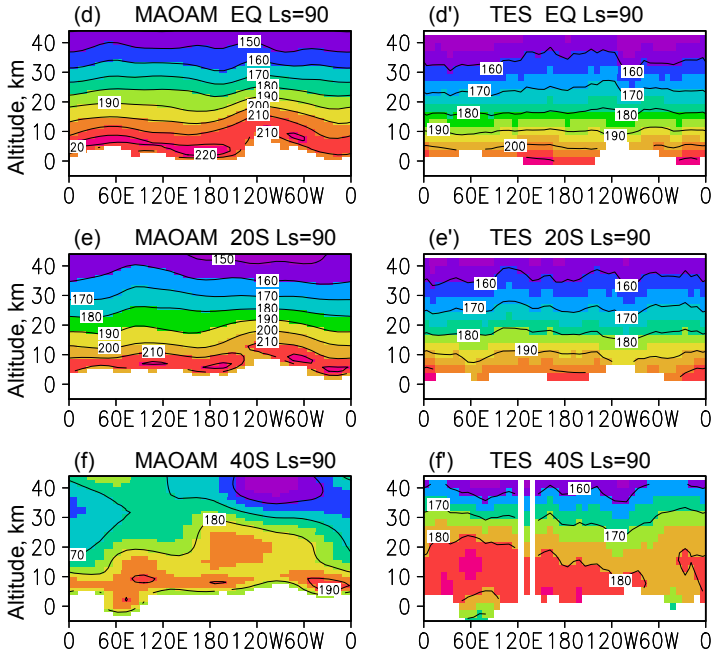


Figure 4.5: Same conditions as in Figure 4.2, but for the other latitudes for $L_s = 90^\circ$.

In this section, we used TES measurements to quantify the relation between T' and I/A . First, we introduce a characteristic value of the thermal inertia, to make the ratio I/A dimensionless by dividing it by I_a . We use $I_a = 300 \text{ J m}^{-2} \text{ K}^{-1} \text{ s}^{-1/2}$, the globally averaged value of the thermal inertia I . Second, we denote

$$\tau \equiv \ln \left(\frac{I}{AI_a} \right). \quad (4.2)$$

Then we assume that the temperature deviation T' and the newly introduced dimensionless variable τ are related as

$$T' = b\tau + a, \quad (4.3)$$

where a and b are the coefficients of the regression to be found from global maps of I , A , and T' by the least mean square method.

Figure 4.6 presents the results of calculations using the TES data for T' , and the distributions of I from [Mellon *et al.*, 2000] and A from [Christensen *et al.*, 2001]. Four panels in Figure 4.6 are for different latitude bands and for different seasons (we present only two solstices $L_s = 90^\circ$ and $L_s = 270^\circ$). Two bottom subpanels (c,d) display longitudinal distributions of τ and T' , correspondingly, and the upper subpanels (a) show the regressions T' versus τ Equation (4.3). As an illustration, the surface topography was plotted in

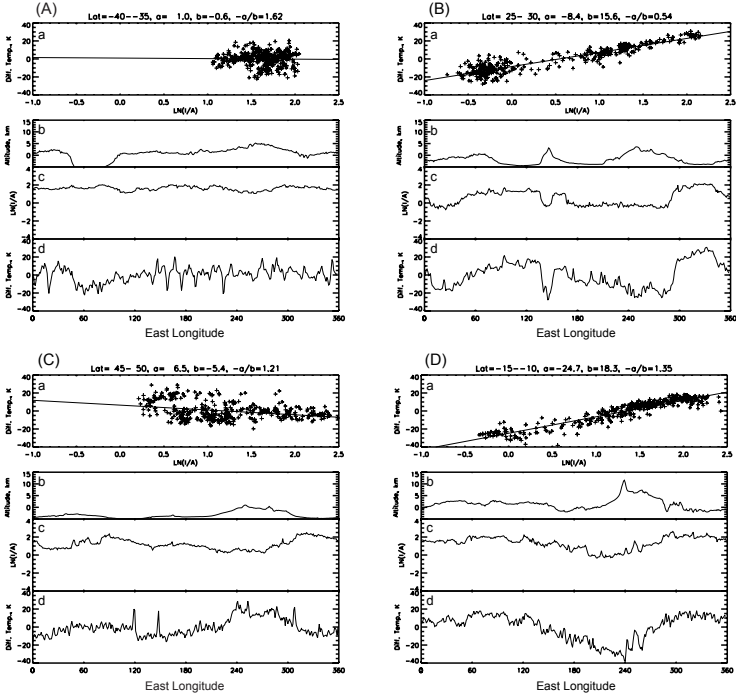


Figure 4.6: Relationship of the surface albedo, thermal inertia, surface temperature observed by MGS-*TES* at low- to mid-latitudes 25°–30°N (B) for $L_s = 90^\circ$, 10°–15°S (D) for $L_s = 270^\circ$, and high latitudes 35°–40°S (A) for $L_s = 90^\circ$, 45°–50°N (C) for $L_s = 270^\circ$. Each panel (A–D) includes four subpanels (a–d). (a) is T^s versus τ following Equation (4.3). (b) is the deviation of topography ($z - \bar{z}^x$). (c) is τ from Equation (4.2). (d) is the surface temperature deviations following Equation (4.1).

subpanels (b). It is qualitatively seen from the two bottom subpanels (c,d) that T^s follows τ to a large degree, and is almost independent of the topography shown in subpanels (b). In the upper subpanels (a), the stars densely gather near the lines of the regression (4.3) whose tilt (i.e. the coefficient b) depends on the latitude and the season. It is interesting that in low- to mid-latitudes, the ratio $-a/b$ approximately remains constant. In other words, the surface temperature disturbance is equal to zero at approximately the same value of τ . However, in mid- to high latitudes, this simple relation fails.

To extend this analysis little further, we notice that A , I , and therefore, τ do not depend on seasons, but T^s does. Figure 4.7a shows the longitudinal standard deviation (rms values) for the surface albedo A and thermal inertia I from 60°S to 60°N. In order

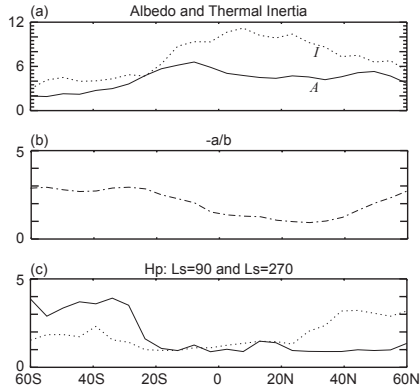


Figure 4.7: (a): The standard deviation of surface albedo $A \times 100^{-1}$ (solid) and thermal inertia $I \times 10$ (dotted). (b): The constant $-a/b$ in Equation (4.3). (c): Root mean square H_p from Equation (4.7) in $L_s = 90^\circ$ (solid), $L_s = 270^\circ$ (dotted).

to estimate how closely (in statistical sense) τ and T' are related, we introduce

$$\tilde{\tau} = \frac{T - \tau_m}{\sigma_\tau}, \quad (4.4)$$

$$\tilde{T}' = \frac{T' - T'_m}{\sigma_{T'}} \quad (4.5)$$

$$(4.6)$$

where the subscript m means longitudinally averaged quantities, and σ_τ and $\sigma_{T'}$ are the rms deviations of the corresponding quantities. Then, the longitudinal standard deviation of the ratio

$$H_p = \frac{\tilde{\tau}}{\tilde{T}'} \quad (4.7)$$

would measure the closeness of surface temperature anomalies T' to the surface characteristics τ . $\text{Rms}(H_p)=1$ would mean a good agreement. The latter quantity is plotted in Figure 4.7c. It shows that $\text{rms}(H_p)$ is close to unity in low- to mid latitudes in both solstices. Therefore, in these latitudes, the surface temperature variations are determined to a large degree by the thermal characteristics of the ground, but very little depend on topography. Of course, the proportionality coefficient depends on a position of the Sun, i.e. on a season.

5 Conclusions

The main task of this work was to study the influence of the surface on the circulation of the Martian atmosphere using a newly developed comprehensive general circulation model (GCM). The main mechanism which provides the vertical coupling between atmospheric layers are planetary waves (PW) and solar tides. These longitudinal disturbances (eddies) are generated near the surface and in the lower atmosphere and propagate upward. Since the air density decreases with height, the amplitudes of the eddies grow accordingly. In the middle and upper atmosphere, PW and tides either break due to the nonlinearity and/or dissipate due to the increasing molecular diffusion. The momentum, energy, and heat carried away by the eddies is then released to the mean flow significantly affecting the general (global) circulation.

Planetary waves are generated in the lower atmosphere due to the flow over the topography or over the surface with varying thermal characteristics. They also are generated due to the instabilities of the mean zonal flow. Solar tides are excited by the diurnal variations in the solar radiation absorption by the carbon dioxide atmosphere, or by the surface with consequent transfer of the energy to the lowest atmospheric layers. Since the Martian surface has a rugged topography with high mountains and deep valleys, planetary wave generation is generally strong in the atmosphere of the Red Planet. Shallower than on Earth the planetary boundary layer provides less dissipation for the generated disturbances. Therefore, eddies are strong in the atmosphere of Mars. Given the low atmospheric density, their influence on the circulation is great.

The main tool used in this work is the general circulation model of the Martian atmosphere. It was developed by joint efforts of several German universities and Max-Planck-Institute for Solar System Research within the framework of the Mars Atmosphere Observations And Modeling (MAOAM) project. The author took part in the development, implementation, and validation of several physical parameterizations: a surface energy budget scheme, a near-IR solar radiation absorption scheme, an LTE longwave radiation parameterization, vertical diffusion and convective adjustment schemes.

A series of numerical simulations was performed to study the sensitivity of the wave generation to the variations of the surface parameters. The response of the global circulation to the changes in wave forcing was investigated. The major conclusion from these numerical experiments is that both solar tides and planetary waves significantly affect the meridional circulation, they even shape it in the middle atmosphere. The effects of solar tides are strong above ≈ 70 km. At these heights, the torque provided to the mean zonal flow by dissipating tides reaches several hundreds $\text{m s}^{-1} \text{ sol}^{-1}$, much stronger than on Earth. Diurnal and semidiurnal components are mostly generated in the lowest 20 km, and selectively propagate upward. Non-dissipating (between 20 and 70 km) tides do not affect the general circulation, as their net effect on the mean flow is zero. In the areas

of a strong dissipation in the mesosphere, the poleward transport gets enhanced. The downward branch of the transport cell over the winter pole is associated with the strong adiabatic heating. This heating is the primary reason for the winter polar warming observed on Mars. The numerical experiments show that large scale longitudinal variations of the surface thermal inertia and albedo increase the semidiurnal component of the tide. They are also the source of quasi-stationary planetary waves. The latter propagate and dissipate/break in a wide range of heights, thus affecting the circulation in both summer and winter hemispheres. The flow over the topography is a more effective generator of planetary waves. Effects of "mechanically" forced planetary waves are strong below ≈ 60 km. The topography also contributes to the generation of the semidiurnal tide. A realistic general circulation can be obtained only when the diurnal variations are included in a combination of the real topography and the observed surface thermal inertia and albedo.

The topography also affects the generation of free modes of atmospheric waves, the traveling planetary waves with periods of several sols. Unlike for stationary PW where the longitudinal variations of the topography are important, the overall South-North slope of the Martian surface determines the strength of traveling PW generation. With the realistic topography, the model reproduces low frequency waves in the $L_s = 270^\circ$ season, and no waves for the $L_s = 90^\circ$ solstice, in accordance with the Viking Lander observations. With the topography reversed symmetrically with respect to the equator, traveling PW generation is inhibited during both seasons. A more close analysis shows that this can be explained by the changes in the atmospheric wave generation and propagation: the realistic topography increases the baroclinic instability of the mean flow and creates more favorable conditions for planetary wave propagation. A series of numerical experiments was performed to study the sensitivity of the mean meridional circulation to the overall pole-to-pole slope in the Martian topography. These experiments showed how a latitudinal position of a steep surface slope affects the formation of Hadley cells depending on a season. Effects of several prominent features on the Martian surface on the local and global circulation were studied in this work. They include the effects of the mountainous region of Mts. Alba, Olympus and Tharsis, nighttime temperature inversions, and the role of both polar ice caps on the wave excitation.

The results of the simulations were compared with the data obtained from Thermal Emission Spectrometer onboard Mars Global Surveyor (TES-MGS). These data cover only heights below 40 km, however provide a global coverage with satisfactory resolution. The simulated zonal mean temperature for different seasons show a good agreement with the observations, especially during dustless seasons. The comparison of the longitudinal disturbances attributed to stationary planetary waves show a qualitative agreement. In part, the differences can be explained by an insufficient vertical resolution of TES near the surface, and by the need for taking a more detailed account of the dust radiation. The TES data were used to establish a simple but statistically significant relation between the surface temperature, thermal inertia and albedo.

A List of Principal Symbols

a	Radius of Mars
a_ν	Absorptance
c_p	Specific heat at constant pressure
c_g	Thermal capacity
d	Mean line spacing
f	Coriolis parameter
g	Acceleration of gravity
k	Karman constant (section 2.2)
k	Thermal conductivity (section 2.4)
l	Mixing length
l_a	Asymptotic mixing length
p	Pressure
u	Zonal wind speed
u	Dimensionless path length (section 2.4)
u'	Eddy deviation from mean zonal wind speed
v	Meridional wind speed
v'	Eddy deviation from mean meridional wind speed
w	Vertical wind speed
w	Optical path (section 2.4)
w'	Eddy deviation from mean vertical wind speed
s_ν	Line strength (Chapter 2)
s	Longitude wavenumber
r	Mars-Sun distance
r_m	Mean Mars-Sun distance
r_\odot	Radius of Sun
t	Time
z	Altitude
A	Surface Albedo
A	Band absorptance (section 2.4.1)
A_0	Effective band width
B_ν	Planck function
D	Atmospheric thickness
E	Turbulent kinetic energy
F_M, F_T	Frictional force (Section 2.1,2.2)
F	Flux

A List of Principal Symbols

H	Scale height
I	Thermal inertia
Kc_i	Baroclinic growth rate
K_c	Coefficient of eddy viscosity
K_m	Heat transfer coefficient
L_s	Solar longitude
N	Brunt-Vaisala frequency
Q	Radiative heating rate
R	Gas constant
R_i	Richardson number
S	Band strength
T	Temperature
T_{\odot}	Blackbody temperature of Sun
β	Mean line width parameter (section 2.4)
β	Latitudinal gradient of the Coriolis parameter
γ_L	Mean line width
ϵ	Emissivity
θ	Potential temperature
θ'	Eddy deviation from mean potential temperature
κ	R/c_p
κ	Thermal diffusivity (section 2.4.3)
λ	Longitude
μ	Cosine of solar zenith angle
ν	Wavenumber
ν	Kinematical viscosity (section 2.4.3)
ρ	Density
σ	Stefan-Boltzmann constant (section 2.4)
σ	Frequency for atmospheric waves
τ	Stress tensor (section 2.2)
τ_{ν}	Transmittance
ϕ	Latitude
φ_c	Static stability function
φ_s	Static stability parameter
ω	Diurnal frequency
Γ	Lapse rate
Θ	Phase
Λ	Wind shear
Φ	Geopotential
Ω	Angular rotation rate of the Mars

Bibliography

- Andrews, D. G., J. R. Holton, and C. B. Leovy (1987), *Middle Atmosphere Dynamics*, Academic Press.
- Andrews, D. G. (2000), *An Introduction to Atmospheric Physics*, Cambridge University Press.
- Barnes, J. R., R. M. Haberle, J. B. Pollack, H. Lee, and J. Schaeffer (1996), Mars atmospheric dynamics as simulated by the NASA Ames general circulation model, 3. Winter quasi-stationary eddies, *J. Geophys. Res.*, *101*, 12753–12776.
- Barnes, J. R., and R. M. Haberle (1996), The Martian zonal-mean circulation: Angular momentum and potential vorticity structure in GCM simulations, *J. Atmos. Sci.*, *53*, 3143–3156.
- Banfield, D., B. Conrath, J. C. Pearl, M. D. Smith, and P. Christensen (2000), Thermal tides and stationary waves on Mars as revealed by Mars Global Surveyor thermal emission spectrometer, *J. Geophys. Res.*, *105*, 9521–9537.
- Banfield, D., B. J. Conrath, M. D. Smith, P. R. Christensen, and R. J. Wilson (2003), Forced waves in the Martian atmosphere from MGS TES nadir data, *Icarus*, *161*, 319–345.
- Banfield, D., B. Conrath, P. J. Gierasch, R. J. Wilson, and M. D. Smith (2004), Traveling waves in the Martian atmosphere from MGS TES Nadir data, *Icarus*, *170*, 365–403.
- Blackadar, A. K. (1962), The vertical distribution of wind and turbulent exchange in a neutral atmosphere, *J. Geophys. Res.*, *67*, 3095–3102.
- Blackadar, A. K. (1979), High-resolution models of the planetary boundary layer, *Adv. Environ. Sci. Eng.*, *1*, 50–85.
- Blumsack, S. L., P. J. Gierasch, and W. R. Wessel (1973), An analytical and numerical study of the Martian planetary boundary layer over slopes, *J. Atmos. Sci.*, *30*, 66–82.
- Cess, R. D., and V. Ramanathan (1972), Radiative transfer in the atmosphere of Mars and that of Venus above the cloud deck, *J. Quant. Spectrosc. Radiat. Transfer.*, *12*, 933–945.
- Christensen, P. R. et al. (2001), Thermal Emission Spectrometer Experiment: Mars Observer Mission, *J. Geophys. Res.*, *97*, 7719–7734.

- Christensen, P. R. et al. (1998), Results from the Mars Global Surveyor Thermal Emission Spectrometer, *Science*, 279, 1692–1698.
- Christensen, P. R. et al. (2001), Mars Global Surveyor Thermal Emission Spectrometer experiment: Investigation description and surface science results, *J. Geophys. Res.*, 106, 23823–23872.
- Colaprete, A., J. R. Barnes, R. M. Haberle, J. L. Hollingsworth, H. H. Kieffer, and T. N. Titus (2005), Albedo of the south pole on Mars determined by topographic forcing of atmosphere dynamics, *Nature*, 435, 184–188.
- Conrath, B., R. Curran, R. Hanel, V. Kunde, W. Maguire, J. Pearl, J. Pirraglia, and J. Welker (1973), Atmospheric and surface properties of Mars obtained by infrared spectroscopy on Mariner 9, *J. Geophys. Res.*, 78, 4267–4278.
- Conrath, B. J., et al. (2000), Mars global surveyor Thermal Emission Spectrometer (TES) observations: Atmospheric temperature during aerobraking and science phasing, *J. Geophys. Res.*, 105, 9509–9520 .
- Crisp, D., S. B. Fels, and M. D. Schwarzkopf (1986), Approximate methods for finding 15- μ m band transmission in planetary atmospheres, *J. Geophys. Res.*, 91, 11851–11866.
- Delacourt, C., N. Gros, P. Allemand, and D. Baratoux (2003), Online Mars digital elevation model derived from MOLA profiles, *EOS Trans. AGU*, 84(52), 583.
- Dickinson, R. E. (1972), Infrared radiative heating and cooling in the Venusian mesosphere. 1: Global mean radiative equilibrium, *J. Atmos. Sci.*, 29, 1531–1556.
- Ebel, A., and U. Berger (1997), Final report. Martian atmosphere – circulation and climate. Mart ACC, *BMBF*.
- Fenton, L. K., and M. I. Richardson (2001), Martian surface winds: Insensitivity to orbital changes and implications for aeolian processes, *J. Geophys. Res.*, 106, 32885–32902.
- Forget, F., G. B. Hansen, and J. B. Pollack (1995), Low brightness temperature of Martian polar caps: CO₂ clouds or low surface emissivity?, *J. Geophys. Res.*, 100, 21219–21234.
- Forget, F., J. B. Pollack (1996), Thermal infrared observations of the condensing Martian polar caps: CO₂ ice temperatures and radiative budget, *J. Geophys. Res.*, 101, 16865–16879.
- Forget, F., F. Hourdin, R. Fournier, C. Hourdin, O. Talagrand, M. Collins, S. R. Lewis, P. Read, and J. Huot (1999), Improved general circulation models of the Martian atmosphere from the surface to above 80 km, *J. Geophys. Res.*, 104, 24155–24175.
- Forget, F., Y. Wanherdick, and S. R. Lewis (2001), *Validation of the Mars General Circulation Model and Climate Database with new spacecraft observations*, Technical note for ESA contract 11369/95/NL/JG, Work Package 7.

- Fukuhara, T., and T. Imamura (2005), Wave encircling the summer southern pole of Mars observed by MGS TES, *Geophys. Res. Lett.*, *32*, 18811, doi:10.1029/2005GL023819.
- Goody, R., and M. J. Belton (1967), Radiative relaxation times for Mars. A discussion of Martian atmospheric dynamics, *Planet. Space. Sci.*, *15*, 247.
- Gierasch, P., and R. Goody (1968), A study of the thermal and dynamical structure of the Martian lower atmosphere, *Planet. Space. Sci.*, *16*, 615–646.
- Haberle, R. M., H. C. Houben, R. Hertenstein, and T. Herdtle (1993), A boundary-layer model for Mars: comparison with Viking Lander and entry data, *J. Atmos. Sci.*, *50*, 1544–1559.
- Haberle, R. M., H. Houben, J. R. Barnes, and R. E. Young (1997), A simplified three-dimensional model for Martian climate studies, *J. Geophys. Res.*, *102*, 9051–9067.
- Haberle, R. M., et al. (1999), General circulation model simulations of the Mars Pathfinder atmospheric structure investigation/meteorology data, *J. Geophys. Res.*, *104*, 8957–8974.
- Hansen, G., M. Giuranna, V. Formisano, S. Fonti, D. Grassi, H. Hirsh, N. Ignatiev, A. Maturilli, P. Orleanski, G. Piccioni, M. Rataj, B. Saggin, and L. Zasova (2005), PFS-MEX observation of ices in the residual south polar cap of Mars, *Planet. Space. Sci.*, *53*, 1089–1095.
- Hartogh, P., A. S. Medvedev, T. Kuroda, R. Saito, G. Villanueva, A. G. Feofilov, A. A. Kutepov, and U. Berger (2005), Description and climatology of a new general circulation model of the Martian atmosphere, *J. Geophys. Res.*, *110*, 11008, doi:10.1029/2005JE002498.
- Hinson, D. P., R. J. Wilson, M. D. Smith, and B. J. Conrath (2003), Stationary planetary waves in the atmosphere of Mars during southern winter, *J. Geophys. Res.*, *108*, 5004, doi:10.1029/2002JE001949.
- Hinson, D. P., and R. J. Wilson (2004), Temperature inversions, thermal tides, and water ice clouds in the Martian tropics, *J. Geophys. Res.*, *109*, 1002, doi:10.1029/2003JE002129.
- Holton, J. R. (1975), *The dynamic meteorology of the stratosphere and mesosphere*, American Meteorological Society.
- Holton, J. R. (1992), *An introduction to dynamic meteorology, 3rd Ed.*, Academic Press.
- Hourdin, F. (1992), A new representation of the absorption by CO₂ 15- μ m band for a Martian General Circulation Model, *J. Geophys. Res.*, *97*, 18319–18335.
- Hourdin, F., F. Forget, and O. Talagrand (1995), The sensitivity of the Martian surface pressure and atmospheric mass budget to various parameters: a comparison between numerical simulations and Viking observations, *J. Geophys. Res.*, *100*, 5501–5523.

- Jakosky, B. M., and R. J. Phillips (2001), Mars' volatile and climate history, *Nature*, *412*, 237–244.
- Joshi, M. M., R. M. Haberle, J. R. Barnes, J. R. Murphy, and J. Schaeffer (1997), Low-level jets in the NASA Ames Mars general circulation model, *J. Geophys. Res.*, *102*, 6511–6523.
- Kieffer, H. H., T. Z. Martin, A. R. Peterfreund, B. M. Jakosky, E. D. Miner, and F. D. Palluconi (1977), Thermal and albedo mapping of Mars during the Viking primary mission, *J. Geophys. Res.*, *82*, 4249–4291.
- Kiehl, J. T., and V. Ramanathan (1983), CO₂ radiative parameterization used in climate models: comparison with narrow band models and with laboratory data, *J. Geophys. Res.*, *88*, 5191–5202.
- Klemp, J. B., and R. B. Wilhelmson (1978), The simulation of three-dimensional convective storm dynamics, *J. Atmos. Sci.*, *35*, 1070–1096.
- Langevin, Y, F. Poulet, J. P. Bibring, and B. Gondet (2005), Sulfates in the north polar region of Mars detected by OMEGA/Mars Express, *Science*, *307*, 1584–1586.
- Leovy, C., and Y. Mintz (1969), Numerical simulation of the atmospheric circulation and climate of Mars, *J. Atmos. Sci.*, *26*, 1167–1190.
- Leovy, C. (2001), Weather and climate on Mars, *Nature*, *412*, 245–249.
- Lewis, S. R., M. Collins, P. L. Read, F. Forget, F. Hourdin, R. Fournier, C. Hourdin, and O. Talagrand (1999), A climate database for Mars, *J. Geophys. Res.*, *104*, 24177–24194.
- Lindzen, R. S., B. Farrell, and K. Tung (1980), The concept of wave overreflection and its application to baroclinic instability, *J. Atmos. Sci.*, *37*, 44–63.
- López-Puertas, M., and M. A. López-Valverde (1995), Radiative energy balance of CO₂ non-LTE infrared emissions in the Martian atmosphere, *Icarus*, *114*, 113–129.
- López-Valverde, M., and D. P. Edwards, M. López-Puertas, C. Roldan (1998), Non-local thermodynamic equilibrium in general circulation models of the Martian atmosphere I. Effects of the local thermodynamic equilibrium approximation on thermal cooling and solar heating, *J. Geophys. Res.*, *103*, 16799–16812.
- Mailhot, J., and R. Benoit (1982), A finite-element model of the atmosphere boundary layer suitable for use with numerical weather prediction model, *J. Atmos. Sci.*, *39*, 2249–2265.
- Manabe, S., and R. F. Strickler (1964), Thermal equilibrium of the atmosphere with a convective adjustment, *J. Atmos. Sci.*, *21*, 361–385.
- Mellon, M. T., B. M. Jakosky, H. H. Kieffer, and P. R. Christensen (2000), High resolution thermal inertia mapping from the Mars Global Surveyor Thermal Emission Spectrometer, *Icarus*, *148*, 437–455.

- Molnar, P., and K. A. Emanuel (1999), Temperature profiles in radiative–convective equilibrium above surfaces at different heights, *J. Geophys. Res.*, *104*, 24265–24271.
- Paige, D. A., and A. P. Ingersoll (1985), Annual heat balance of Martian polar caps - Viking observations, *Science*, *228*, 1160–1168.
- Paige, D. A., J. E. Bachman and K. D. Keegan (1994), Thermal and albedo mapping of the polar regions of Mars using Viking thermal mapper observations 1. North polar region, *J. Geophys. Res.*, *99*, 25959–25991.
- Paige, D. A., and K. D. Keegan (1994), Thermal and albedo mapping of the polar regions of Mars using Viking thermal mapper observations 2. South polar region, *J. Geophys. Res.*, *99*, 25993–26013.
- Pickersgill, A. O. (1984), Martian bore waves of the Tharsis region: a comparison with Australian atmospheric waves of elevation, *J. Atmos. Sci.*, *41*, 1461–1473.
- Pollack, J. B., C. B. Leovy, P. W. Greiman, and Y. Mintz (1981), A Martian general circulation experiment with large topography, *J. Atmos. Sci.*, *38*, 3–29.
- Pollack, J. B., R. M. Haberle, J. Schaeffer, and H. Lee (1990), Simulations of the general circulation of the Martian atmosphere 1. polar processes, *J. Geophys. Res.*, *95*, 1447–1473.
- Pollack, J. B., R. M. Haberle, and J. R. Murphy (1993), Simulations of the general circulation of the Martian atmosphere 2. Seasonal pressure variations, *J. Geophys. Res.*, *98*, 3149–3181.
- Putzig, N. E., M. T. Mellon, K. A. Kretke, and R. E. Arvidson (2005), Global thermal inertia and surface properties of Mars from the MGS mapping mission, *Icarus*, *173*, 325–341.
- Ramanathan, D., and R. D. Cess (1974), Radiative transfer within the mesosphere of Venus and Mars, *Astrophysical Journal*, *188*, 407–416.
- Ramanathan, V. (1976), Radiative transfer within the Earth's troposphere and stratosphere: A simplified radiative-convective model, *J. Atmos. Sci.*, *33*, 1330–1346.
- Ramanathan, V., and J. A. Coakley (1978), Climate modeling through radiative-convective models, *Rev. Geophys. Space Phys.*, *16*, 465–489.
- Richardson, M. I., and R. J. Willson (2002), A topographically forced asymmetry in the Martian circulation and climate, *Nature*, *416*, 298–300.
- Ringler, T. D., and K. H. Cook (1999), Understanding the seasonality of orographically forced stationary waves: Interaction between mechanical and thermal forcing, *J. Atmos. Sci.*, *56*, 1154–1174.
- Santee, M. L., and D. Crisp (1995), Diagnostic calculations of the circulation in the Martian atmosphere, *J. Geophys. Res.*, *100*, 5465–5484.

- Smith, D. E., and M. T. Zuber (1996), The shape of Mars and the topographic signature of the hemispheric dichotomy, *Science*, *271*, 184–188.
- Smith, D. E., et al. (1999), The global topography of Mars and implications for surface evolution, *Science*, *284*, 1495–1503.
- Smith, D. E., M. T. Zuber, R. M. Haberle, D. D. Rowlands, and J. R. Murphy (1999), The Mars seasonal CO₂ cycle and the time variation of the gravity field: A general circulation model simulation, *J. Geophys. Res.*, *104*, 1885–1896.
- Smith, M. D. (2004), Interannual variability in TES atmospheric observations of Mars during 1999–2003, *Icarus*, *167*, 148–165.
- Stull, R. B. (1997), *An Introduction to Boundary Layer Meteorology*, 254 pp., Kluwer Academic Publishers.
- Sutherland, R. A., J. F. Bartholic, and J. F. Gerber (1979), Emissivity correction for interpreting thermal radiation from a terrestrial surface, *J. Appl. Meteorol.*, *18*, 1165–1171.
- Sutton, J. L., C. B. Leovy, and J. E. Tillman (1978), Diurnal variations of the Martian surface layer meteorological parameters during the first 45 sols at two Viking Lander sites, *J. Atmos. Sci.*, *35*, 2346–2355.
- Takahashi, Y. O., H. Fujiwara, H. Fukunishi, M. Odaka, Y. Hayashi, and S. Watanabe (2003), Topographically induced north-south asymmetry of the meridional circulation in the Martian atmosphere, *J. Geophys. Res.*, *108*, 5018, doi:10.1029/2001JE001638.
- Takayabu, I., and S. Takehiro (2003), Wave over-reflection and baroclinic instability of the eddy problem, *J. Atmos. Sci.*, *60*, 2404–2412.
- Villanueva, G. (2004), The high resolution spectrometer for SOFIA-GREAT instrumentation, atmospheric modeling and observations, Ph.D. thesis, Univ. of Freiburg, Germany.
- Warren, S. G. (1986), Optical constants of carbon dioxide ice, *Applied Optics*, *25*, 2650–2674.
- Wilson, R. J., and K. Hamilton (1996), Comprehensive model simulation of thermal tides in the Martian atmosphere, *J. Atmos. Sci.*, *53*, 1290–1326.
- Wilson, R. J. (1997), A general circulation model simulation of the Martian polar warming, *Geophys. Res. Lett.*, *24*, 123–126.
- Zhang, D., and R. A. Anthes (1982), A high-resolution model of the planetary boundary layer—sensitivity tests and comparisons with SESAME-79 data, *J. Appl. Meteorol.*, *21*, 1594–1609.
- Zhang, K. Q., A. P. Ingersoll, D. M. Kass, J. C. Pearl, M. D. Smith, B. J. Conrath, and R. M. Haberle (2001), Assimilation of Mars Global Surveyor atmospheric temperature data into a general circulation model, *J. Geophys. Res.*, *106*, 32863–32877.

- Zurek, R. W. (1985), The form of Newtonian cooling in atmospheric tidal theory, *Pa-geoph*, 123, 921–929.
- Zurek, R. W. (1992), *Comparative aspects of the climate on Mars: an introduction to the current atmosphere, Mars*, Arizona press.

Acknowledgements

I thank my advisor, Paul Hartogh, for giving me the opportunity to work in a very interesting area, and for his support and guidance throughout my studies at Max-Planck-Institute for Solar System Research. I thank Alexander Medvedev for suggesting that I take on this study and for his invaluable comments. I thank the members of my committee for their time and effort for the financial support of my work. I thank Geronimo, Takeshi and many other stuff for their invaluable help during the MAOAM project. I thank all the friends I have met over my about 3 years at Lindau. I thank my mother for her love and support while I decided to be a professional student for a while. I learned a great deal from each of you.

Ryu Saito: Influence of the Surface on the Atmospheric Circulation of Mars: Study with a General Circulation Model

Unlike on Earth where 3/4 of the surface is covered by oceans, the Martian surface has rougher topography with greater magnitudes of mountains and valleys. The Martian atmosphere is less dense compared to the terrestrial one. The planetary boundary layer is significantly shallower on Mars than on Earth. These differences indicate that the Martian atmosphere should be very sensitive to the forcing from below. The major mechanism which provides vertical coupling are atmospheric waves generated in the lower atmosphere near the surface. These waves transport the momentum, energy, and heat away from places of their generation in the lower atmosphere. Propagating upward the wave disturbances grow in amplitude, and ultimately break or dissipate. They release the wave energy and momentum to the zonal mean circulation, and thus affect the global transport in the atmosphere of Mars. The main task of this work is to study various physical phenomena which take place in the atmosphere near the surface with an emphasis on the mechanisms of wave generation. Effects of the large scale longitudinal disturbances on the general circulation, especially in the upper and middle atmosphere, are explored. Results of numerical experiments with the General Circulation Model of the Martian Atmosphere (MAOAM) show the sensitivity of the zonal mean circulation to the surface properties. Planetary waves of different scales are generated by a flow over the topography as well as by the inhomogeneous reaction of the surface and the lower atmospheric layers to the solar heating. Solar tides are excited by the diurnal variations in the solar energy absorption by the air, and especially, by the surface. These large scale disturbances propagate upward and horizontally according to the selective transmission properties of the atmosphere, and redistribute the wave momentum and energy. Breaking waves provide a torque to the mean zonal wind and maintain the global meridional transport. The results of the numerical simulations showing the sensitivity of the polar night jet to the topography, the inhomogeneous thermal inertia and the surface albedo, are presented here. In order to validate the simulations, the numerical results are compared with observations from the Thermal Emission Spectrometer (TES) onboard the Mars Global Surveyor (MGS). This work was a part of the ongoing Martian Atmosphere Observations And Modeling (MAOAM) project to develop and validate a comprehensive state-of-the-art general circulation model of the Martian atmosphere.